

Moisture Sensitive Smart Yarns and Textiles from Self-Balanced Silk Fiber Muscles

Tianjiao Jia, Yang Wang, Yuanyuan Dou, Yaowang Li, Monica Jung de Andrade, Run Wang, Shaoli Fang, Jingjing Li, Zhou Yu, Rui Qiao, Zhuangjian Liu, Yuan Cheng, Yewang Su, Majid Minary-Jolandan, Ray H. Baughman, Dong Qian, and Zunfeng Liu*

Smart textiles that sense, interact, and adapt to environmental stimuli have provided exciting new opportunities for a variety of applications. However, current advances have largely remained at the research stage due to the high cost, complexity of manufacturing, and uncomfortableness of environment-sensitive materials. In contrast, natural textile materials are more attractive for smart textiles due to their merits in terms of low cost and comfortability. Here, water fog and humidity-driven torsional and tensile actuation of thermally set twisted, coiled, plied silk fibers, and weave textiles from these silk fibers are reported. When exposed to water fog, the torsional silk fiber provides a fully reversible torsional stroke of $547^\circ \text{ mm}^{-1}$. Coiled-and-thermoset silk yarns provide a 70% contraction when the relative humidity is changed from 20% to 80%. Such an excellent actuation behavior originates from water absorption-induced loss of hydrogen bonds within the silk proteins and the associated structural transformation, which are corroborated by atomistic and macroscopic characterization of silk and molecular dynamics simulations. With its large abundance, cost-effectiveness, and comfortability for wearing, the silk muscles will open up additional possibilities in industrial applications, such as smart textiles and soft robotics.

1. Introduction

The global smart textile industry is estimated to be worth more than \$130 billion by 2025 according to a recent report,^[1] and big tech companies from health-care, sports, fashion, and IT are already investing on it. Exciting progresses have been made on developing smart textiles and bring the traditional textile industry to a high technological level. Novel fabrics that integrate extra functionalities for the end user (such as in providing energy storage,^[2] energy harvesting,^[3] self-cleaning,^[4] sensing,^[5] color change,^[6] light emission,^[7] and temperature,^[8] and moisture regulation^[9]) are dictating the fourth textile/fashion industrial revolution.^[1] In particular, moisture-responsive textiles that can change porosity by adapting to perspiration, rain, humidity, and temperature are of special interest for providing increased comfort for the wearer, through

T. Jia, Y. Dou, J. Li, Prof. Z. Liu
State Key Laboratory of Medicinal Chemical Biology
Key Laboratory of Functional Polymer Materials
College of Pharmacy
Nankai University
Tianjin 300071, China
E-mail: liuzunfeng@nankai.edu.cn

Y. Wang, Prof. D. Qian, Prof. M. Minary-Jolandan
Department of Mechanical Engineering
University of Texas at Dallas
Richardson, TX 75080, USA

Dr. Y. Li
School of Life Sciences
Tsinghua University
Beijing 100084, China

Dr. M. Jung de Andrade, Dr. S. Fang, Prof. R. H. Baughman
Alan G. MacDiarmid NanoTech Institute
University of Texas at Dallas
Richardson, TX 75080, USA

R. Wang
College of Electronic Information and Optics Engineering
Nankai University
Tianjin 300071, China

Z. Yu, Prof. R. Qiao
Center for Soft Matter and Biological Physics
Virginia Tech
Blacksburg, VA 24061, USA

Prof. Z. Liu, Prof. Y. Cheng
Institute of High Performance Computing
Agency for Science Technology and Research (A*STAR)
Singapore 138632, Singapore

Prof. Y. Su
State Key Laboratory of Nonlinear Mechanics
Institute of Mechanics
Chinese Academy of Sciences
Beijing 100190, China

Prof. Y. Su
School of Engineering Science
University of Chinese Academy of Sciences
Beijing 100049, China

Prof. Y. Su
Beijing Key Laboratory of Engineered Construction and Mechanobiology
Institute of Mechanics
Chinese Academy of Sciences
Beijing 100190, China

 The ORCID identification number(s) for the author(s) of this article can be found under <https://doi.org/10.1002/adfm.201808241>.

DOI: 10.1002/adfm.201808241

moisture and thermal management. The incorporation of traditional textile technology and fiber artificial muscles is an effective method to realize these multiple advanced functionalities of smart textiles.^[10]

Various types of fiber artificial muscles based on twisted and coiled yarns have been reported, which can provide fast, large-angle torsional actuation and giant tensile actuation in response to the various stimulus, including temperature, moisture/perspiration, light, pH, etc., that are driven by the mechanism of fiber volume expansion.^[11] An advantage of fiber-like artificial muscles with helical configuration is that the twisting technique used for preparing fiber muscles is a commonly used processing method in textile industry.^[12] Oriented fibers from polyethylene, nylon,^[13] graphene,^[11a] and carbon nanotubes^[11b] have been reported to be used as fiber artificial muscles based on the twisting technique. However, currently these materials are difficult to be commercialized as smart textiles for wearing, because either they are costly and involve complex manufacturing chemical processes (in the case of graphene and carbon nanotube fibers), or they cannot provide a comfortable wearing experience and do not respond to humidity for the purpose of managing body temperature (in the case of polyethylene and nylon fibers). By contrast, natural textile materials are already widely used as textiles due to their merits in terms of low cost and comfortability. In addition, twisted textile fibers from naturally aligned nanofibers have demonstrated good mechanical strength or dyeability, such as silk^[14] or cellulose fibers fabricated either via a bottom-up or top-down approach.^[15] However, to the best of our knowledge, there has been no report on application of twist-based artificial muscles prepared from natural fibers that are widely used in textile industry in the fabrication of smart textiles, which can respond to humidity and used for heat management.

Bombyx mori silk (silkworm silk), one of the most highly engineered natural fibers,^[16] attracts much attention from the textile industry and scientific community because of its outstanding mechanical properties,^[17] hygroscopicity,^[16] biocompatibility^[18] with human body, lightweight, and low cost (≈ 50 USD per kg for processed silk yarns). Hygroscopicity results in gigantic volume expansion of silk upon water absorption,^[17] indicating that silk would be a promising candidate for this twist-based artificial muscles. In addition, mature processing methods of silk, such as degumming,^[19] spinning, twisting, weaving,^[20] dyeing,^[21] and thermal setting, ensure the extensive applicability of silk fibers to the twist-based artificial muscle fabrication for smart textiles.

In this work, we demonstrate water fog/humidity driven torsional and tensile actuation of thermally set, twisted, coiled, and plied silk fibers, weave textiles from these silk fibers, and textile actuation. To enable reversible actuation without the need for torsional tethering, we exploit torque-balanced fiber structures that are obtained by folding a twisted fiber onto itself (by bending at fiber midpoint), which results in fiber plying. When exposed to water fog, the torsional muscle provided a fully reversible torsional stroke of $547^\circ \text{ mm}^{-1}$, which was close to the torsional stroke reported for a moisture-driven twisted graphene fiber ($588.6^\circ \text{ mm}^{-1}$),^[11a] and nine times that of a water-absorption-driven coiled carbon-nanotube fiber ($61.3^\circ \text{ mm}^{-1}$).^[22] Coiled-and-thermoset silk fibers provided a

70% contraction when the relative humidity (RH) was changed from 20% to 80%, which was larger than for a coiled CNT yarn driven by organic solvents (60%).^[23] Molecular dynamics simulation revealed that loss of hydrogen bonds within the silk protein and the associated structural transformation were mainly responsible for the experimentally realized water-driven activation. From the application perspective, these muscles can be used for moisture-sensitive smart textiles and walking robots.

2. Results and Discussions

2.1. Silk Structure and Properties

Raw silk fiber is spun from the two glands of silkworm and is composed of two primary filaments, called brin, which comprises fibroin proteins. The brins are glued together to form a bave with sericin proteins, which also serve as an adhesive to construct the overall structure of the cocoon (Figure S1, Supporting Information).^[16,24] The two fibroin filaments near fiber center are bound together and over coated with the sericin. The fibroin consists of highly ordered beta pleated sheets (β -sheets), which assemble because of strong hydrogen bonding and salt linkages between the side groups of the polypeptide chains.^[25] These structural characteristics result in excellent mechanical properties of silk. The large number of amino acids containing hydrophilic groups contribute to the hygroscopic nature of silk fiber, providing silk's ability to absorb up to 40% moisture when exposed to atmospheric conditions.^[16] These properties make silk an ideal candidate for the preparation of moisture-actuated artificial muscles for smart textile applications.

The sericin protein contains a larger number of hydrophilic groups, and these protein molecules are not closely arranged,^[16] so water molecules can easily penetrate through the sericin sheath to reach the fibroin core. However, removal of the sericin sheath by degumming facilitates the water transport into the fibroin, and the associated volume changes are exploited for the present silk muscles.

In order to free the silk filaments from sericin, a reeling process was operated in hot water to unwrap the silk cocoon to provide silk fiber, and then sericin was removed by placing raw silk fibers in acidic or basic solutions, during the so-called degumming process. As shown in Figure S2 of the Supporting Information, the effect of degumming using H_2SO_4 and NaOH solutions was investigated. While degumming using a H_2SO_4 solution was not sufficient to completely remove sericin from surfaces of the fibroin filaments, degumming with NaOH solution enabled most of the sericin to be removed, and surfaces of the two neighboring fibroin filaments in the resulting silk became smooth.

Further characterizations were conducted on the influence of degumming on the structure and properties of the silk. According to the Fourier transform infrared (FTIR) spectra, the X-ray diffraction (XRD) patterns and thermal gravimetric (TG) analysis scans (Figures S3–S5), degumming did not significantly affect the structure and thermal stability of the silk fiber. Importantly, for actuator applications, the force–displacement curves of Figure S6a of the Supporting Information show that reduction of silk fiber diameter by sericin removal did not

dramatically decrease the rupture force or the initial force constant for elastic deformation. Moreover, the stress–strain curves of Figure S6b of the Supporting Information show that reduction in sericin content by degumming increased fiber fracture stress and slightly decreased the failure strain.

Due to the high density of hydrophilic groups (such as $-\text{COOH}$, $-\text{NH}_2$, and $-\text{OH}$) and the nanopores in the silk fiber,^[26] water molecules can easily be absorbed into silk fibroin. At the maximum water uptake, the silk fiber increased volume by about 34% and increased diameter by about 15%, but increased length by only about 1% (Figure S7, Supporting Information).^[16] Such a giant volume expansion via water absorption would enable the possibility of fabrication of tensile and torsional artificial muscles with large stroke via a twist-insertion technique.

The interaction of water with silk proteins has been an active topic of study in recent years and great progress has been achieved,^[27] while mechanisms behind water absorption and desorption of silk fiber remains poorly understood. In order to understand the fundamental mechanisms responsible for the observed volume expansion in the point of view of protein structural changes, different techniques including molecular dynamics simulations, 2D X-ray diffraction experiments, and measurement of the kinetics of water absorption were performed on *bombyx mori* silk fibroin proteins.

For molecular dynamics simulations, structures of silk fibroin proteins were generated based on Protein Data Bank Entry (PID: 3UA0) and two conditions, i.e., vacuum (fully dehydrated) and fully hydrated were simulated. The 3UA0 represents the N-terminal of the silk fibroin and is a highly ordered system containing mostly β -sheets. By comparing the 3UA0 model before and after hydration, it was observed that water promoted the formation of hydrogen bonds with the hydrophilic groups ($-\text{NH}_2$ or $-\text{OH}$ in the residues of ASP, TYR, THR, GLN, ASN, ARG, LYS, SER, and GLU) in silk fibroin, which provided a competition mechanism with the original inter- and intrachain hydrogen bonds. As a result, the total number of protein hydrogen bonds decreased (Figure S8, Supporting Information). This loss of chain–chain hydrogen bond interaction led to expansion of the system and reduction of the interaction energy within the protein (Figure S9, Supporting Information). The volume expansion was also evidenced by the increasing gyration radius (Figure S10, Supporting Information) and the volume of the model as shown in Table S1 of the Supporting Information. Similar results were also obtained for another two relatively disordered protein chains (PIDs: 3PUB and 2FJY) containing different ratio of α -helices and β -sheets, which are extracted from silkworms rather than silk fibroin (Figures S8–S10, Supporting Information).

Another important finding is that water also led to the transformation from random coil to ordered secondary structure that featured a mixture of both α -helices and β -sheets (Table S2, Supporting Information). The result also displays that the protein structure became regular locally. The simulation result manifests that more amino acid residues turned into the part of secondary structures: short helix transformed to a longer helix, loop transformed to β -sheets or α -helices (Figure 1a; Figure S11, Supporting Information). These observations were quantified by a count on the amino acid residues that

formed the secondary structure, which shows addition of water molecules led to an increase in amino acid residues (Table S1, Supporting Information). Although the number of hydrogen bonds in the secondary structures increased, the total number of hydrogen bonds decreased due to the dramatic reduction of hydrogen bonds in the rest regions of the protein structure due to water absorption. The simulation findings suggested that water worked as plasticizer and enhanced the mobility of silk fibroin. As such, the chains were provided a path way to slide and unwind to transform from messy random-coil to ordered secondary structure.^[27a] X-ray diffraction experiments further confirmed structure change of proteins in silk fiber after hydration. Many diffraction peaks of dry silk spread with a wide range on the ring of the resolution 4.44 Å (Figure 1b), while peaks of wet silk were found with a narrow range on the ring at the same resolution and some strong diffraction peaks appeared at resolution 3.22 Å (Figure 1c). These results indicated that protein structure in the fiber rearranged more regularly. The emerged lattice with distance 3.22 Å demonstrated that some atoms of protein rearranged largely on this order. This provided plausible evidence on the new hydrogen bonds formed in protein structure since the interatomic distance of the hydrogen bond donor and acceptor is about 3.2 Å. Further, we can infer that more secondary structures (α -helices or β -sheets) formed after hydration in silk fiber, in accordance with the molecular dynamics simulations.

Based on the XRD data and simulation results, it is shown that water molecules can facilitate assembly of longer β -sheets. This finding is further supported by the mechanical property change of silk fibroin induced by humidity as shown in Figure 1d, where higher humidity leads to lower fracture stress (as a result of longer β -sheets). This structural–mechanical property correlation is consistent with earlier report,^[30] where it was revealed through both experimental and theoretical studies that an increase in β -sheet nanocrystal size leads to loss of strength of silk fibril.^[28]

The idea that water absorption is accompanied by structural change in the silk fiber is further corroborated by our measurement of the kinetics of water absorption. When a dry silk fiber is exposed to air with a relative humidity of 60%, its uptake of water ($M_w(t)$) scales as $M_w(t) \sim t^{0.87}$ at short time (t) (see Figure 1e). The exponent 0.87 is in excellent agreement with the exponent of 0.89 expected for the scaling of the uptake of penetrants into glassy polymers through the Case II diffusion,^[29] where the absorbed penetrant molecules plasticize and swell the glassy polymers.^[30] The hysteresis of water absorption–desorption during the cyclic exposure of the silk fiber to water fog of high and low relative humidity is limited. This helps to ensure the reversible expansion and contraction of the silk fiber, which can be harnessed to produce highly reversible strokes of the silk muscle.

2.2. Fabrication of Torsional Silk Muscles

In order to dramatically increase muscle stroke during reversible water absorption and desorption, the degummed silk fibers were twist-inserted as schematically shown in Figure 2a. The twisted fiber that was mechanically unstable and tend to untwist was folded at the middle, and the two parts of the fiber

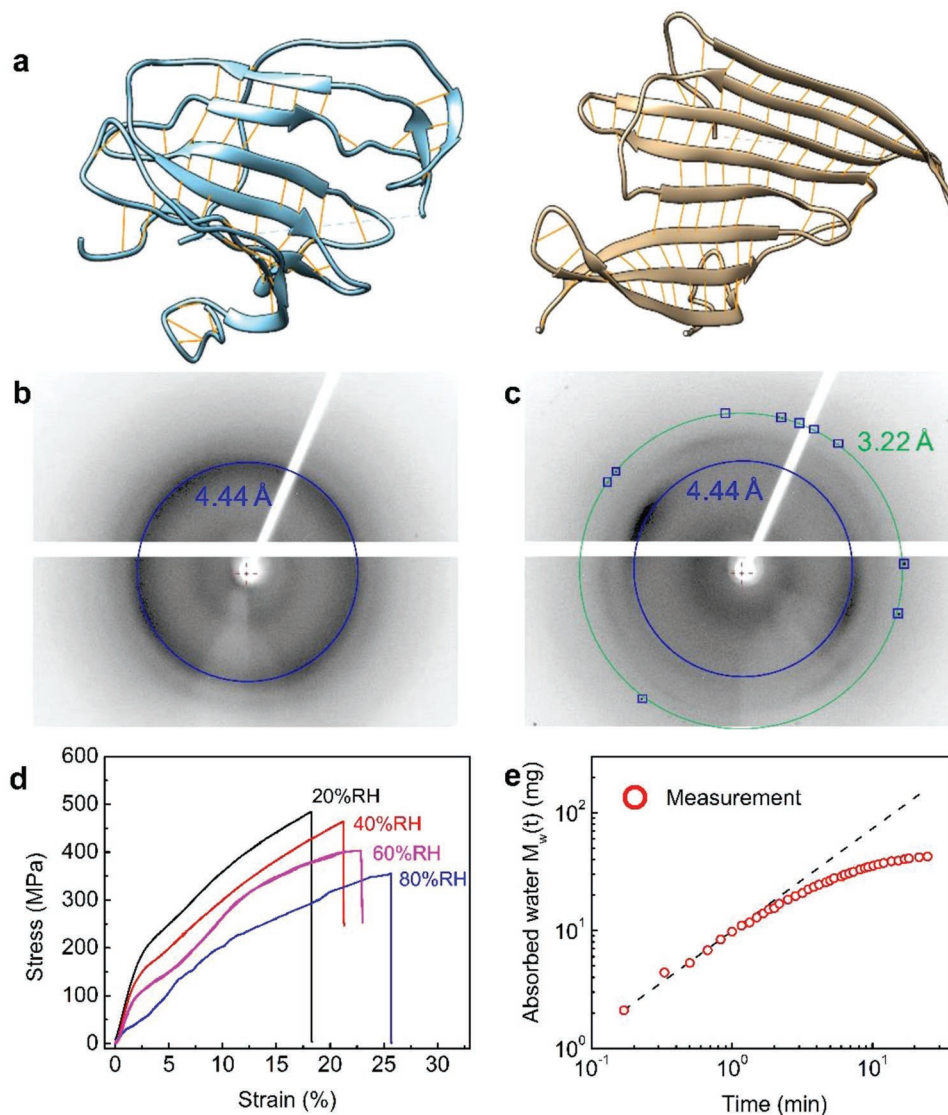


Figure 1. a) Molecular dynamic simulation of the proteins (pdb ID is 3UA0) before and after water molecules added. The simulation result of protein 3UA0 shows the loop structure undergoes transition into a protein secondary structure. In addition, the structure becomes more regular. X-ray diffraction experiment of silk fiber b) before and c) after water absorbed (X-ray source: MicroMax 007 HF). d) Representative stress–strain curves for dual-filament alkali-degummed nontwisted fibers under different ambient humidities at 25 °C. e) Kinetics of the water uptake by a silk fiber. The initially dried silk fiber was introduced into a chamber with an RH of 60% and its weight gain due to the water absorption was monitored. The dashed line indicates a power law scaling with an exponent of 0.87.

were then plied together under an attached load by allowing untwist of the initially twisted fiber to provide the twist of plying that makes a torque-balanced torsional silk muscle. So the direction of plying was opposite to the direction of twist of the individual fiber. Figure S12 of the Supporting Information shows the twist of plying to provide a torque balanced structure (under the indicated isobaric load) as function of the twist inserted in the initial fiber. If the individual fiber has a twist direction of S (a left-handed twist), the plying direction of the two parts of the fiber is Z (a right-handed twist), and the self-balanced torsional silk muscle is then labeled as S (according to the twist direction of the individual fiber).

Upon absorption of water molecules, each of the individual fiber segments with S twist will untwist because of expansion

in fiber volume, which produces a torque, and leads to increase of the plying of the two fibers in Z direction because the direction of plying was opposite to the direction of twist of the fiber. Water desorption causes these processes to reverse (Figure 2a).

During torsional actuation, a paddle was placed at the end of the two-ply torsional muscle, which provided the isobaric load and facilitated measurement of torsional actuation. From the SEM images of silk fiber after alkali degumming (Figure 2b), the diameter of each of the two fibers resulting from degumming the neat silk fiber was about 8 μm . Fibers of this type were processed, as described, Z-twisted silk fiber was made by twisting one dual-filament fiber as shown in Figure 2c. Figure 2d,e shows silk muscles twisted from one and three dual-filament fibers, which diameters were about 27 and 63 μm , respectively.

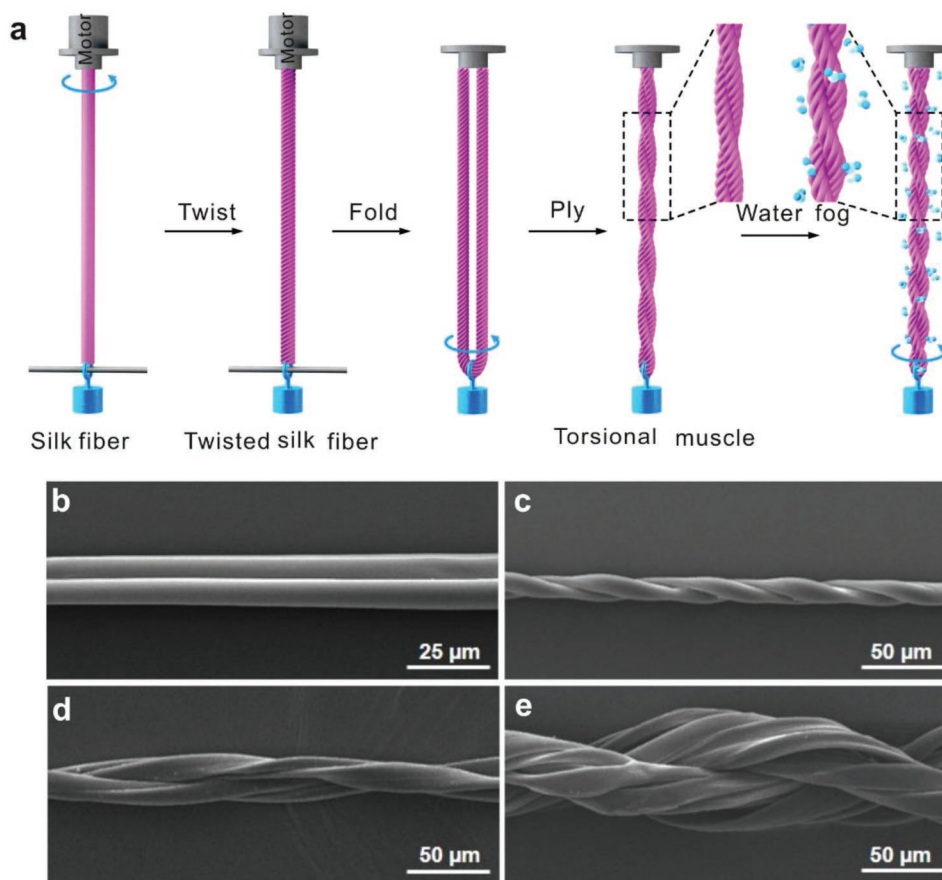


Figure 2. a) Schematic illustration of the fabrication of a two-ply, torque-balanced silk torsional muscle. SEM images of alkali-treatment-degummed b) nontwisted and c) twisted dual-filament fibers, silk muscles twisted from d) one and e) three dual-filament fibers, respectively. The twist densities b–e) are 0, 8000, 6000, and 6000 turns m^{-1} , respectively, when normalized with respect to the nontwisted length.

Torsional silk muscles generate a reversible torsional stroke during humidity changes or upon exposure to ultrasonically generated fog in an open circulating environment (20% RH, 25 °C). Unless otherwise specified, actuation was driven by exposure of the silk muscle to this fog, which was generated by the ultrasonic cavitation of water. Removal of this fog reversed actuation. Also, unless otherwise indicated, the investigated muscle was made from a single dual-filament alkali-degummed twisted fiber by the process illustrated in Figure 2a. A high speed camera was used to record torsional rotation, which was then interpreted by frame-by-frame analysis.

2.3. Torsional Actuation of Silk Muscles

Figure 3a shows the time dependence of torsional stroke and rotation speed during cycles in which water fog was delivered for 15 s and then removed for 18 s when the fog was interrupted. The investigated 10-cm-long, $\approx 19 \mu m$ diameter muscle (weighing 45.8 μg) was two-ply and torque balanced, and was made (using the process of Figure 2a) from two parallel fibroin filaments that had been twisted together using 9000 turns m^{-1} of twist. The speed of the rotation during water absorption correlate with the mass uptake of

water was shown in Figure S13 of the Supporting Information. The torsional silk muscle provided highly reversible torsional actuation during the investigated 500 cycles. The forward and reverse rotation speed was fairly stable, and ratio of forward-to-reverse rotation speed was close to 0.8 (Figure 3b). After 500 cycles, the maximum rotation had no significant decrease, the variation of rotation rate was within 10% (Figure S14, Supporting Information). The maximum torsional rotation rate observed was 975 rpm (102 rad s^{-1}), and the fiber rotated by 425° mm^{-1} . Considering the moment of inertia (6×10^{-11} kg m) of the 50 mg mass paddle (which was a thousand times heavier than the muscle) and the maximum observed torsional acceleration, the generated torque per muscle mass was 63.0 mN $m kg^{-1}$. The above torsional stroke (425° mm^{-1}) and specific torque generated (63.0 mN $m kg^{-1}$) for silk muscles are similar to the torsional rotation (588° mm^{-1}) and specific torque (82 mN $m kg^{-1}$) reported for a humidity-driven, twisted graphene oxide fiber^[11a] (Table S3, Supporting Information). Compared to muscles produced using untreated or H_2SO_4 -degummed silk filaments, NaOH-degummed silk muscles provided optimal torsional performance (Figure S15, Supporting Information).

The ability of fiber volume expansion to drive fiber untwist depends on the bias angle of the silk fibroin with respect

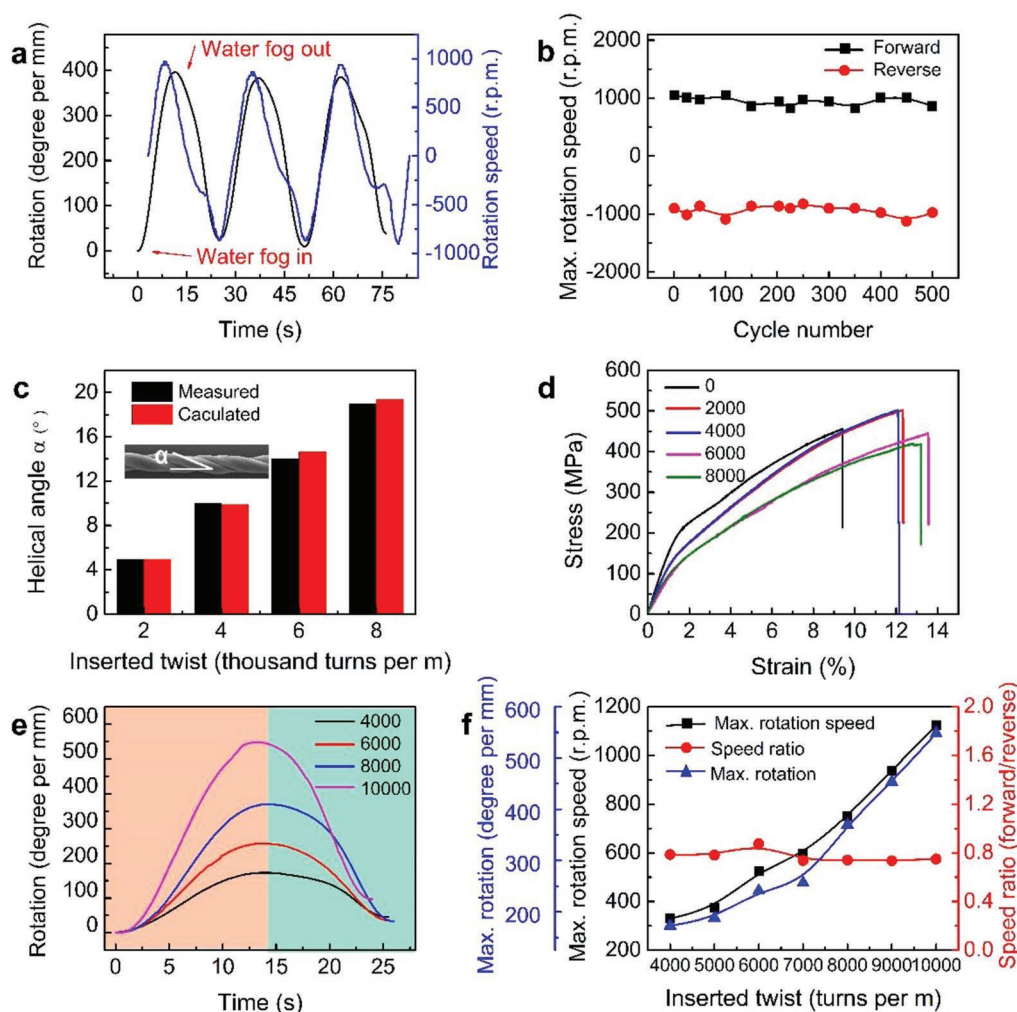


Figure 3. a) Time dependence of torsional actuation and rotation speed for a torsional silk muscle. b) Cycling test showing the change of maximum rotation speed during actuation cycles in which the torsional silk muscle was exposed to ultrasonically generated fog (black squares) and then delivery of the fog was interrupted (red circles). c) Dependence of bias angle α on the amount of inserted twist (black bars: measured and red bars: calculated) for a single dual-filament twisted silk fiber. d) Stress–strain curves for dual-filament alkali-degummed twisted fibers with different twist densities under ambient conditions of $\approx 10\%$ RH at 25°C . e) Time dependence of torsional actuation for silk muscles having different amount of inserted twist in turns m^{-1} . f) Dependence of maximum rotation speed, torsional stroke, and speed ratio on the amount of inserted twist. The speed ratio is equal to the maximum rotation speed during untwisting over that of maximum rotation speed of twisting. All the investigated torsional silk muscles were made (using the process of Figure 2a) from a single alkali-degummed dual-filament silk fiber (10 cm long and $19\ \mu\text{m}$ in diameter) that were two-ply and torque balanced. The twist density for (a) and (b) was $9000\ \text{turns m}^{-1}$. The paddle weight was $50.0\ \text{mg}$.

to the fiber direction,^[11b,31] which can be approximately expressed as

$$\alpha_{\text{fibrin}} = \tan^{-1}(2\pi rT) \quad (1)$$

where r is the radial distance from fiber center and T is the amount of inserted twist per initial fiber length. As shown in Figure 3c, the bias angles obtained using SEM measurements for silk fibers with different amount of inserted twist (Figure S16, Supporting Information) agree well with the calculated results using Equation (1). The representative stress–strain curves for silk fibers having different amount of inserted twist are shown in Figure 3d. These results indicate that the failure strain increased and the breaking strength decreased slightly with increasing the amount of inserted twist (Figure S17, Supporting Information).

Figure 3e shows, during a single actuation cycle, the time dependence of water fog-driven torsional actuation for silk muscles having different amounts of inserted twist. The investigated 10-cm-long, $\approx 19\ \mu\text{m}$ diameter muscles (weighing $45.8\ \mu\text{g}$) were two-ply and torque balanced, and were made (using the process of Figure 2a) from dual-filament silk fibers. As shown in Figure 3f, both torsional stroke and rotation speed increased monotonically with increasing inserted twist. The torsional stroke and rotation speed increased from 173 to $547^\circ\ \text{mm}^{-1}$ and from 330 to $1125\ \text{rpm}$, respectively, when twist density increased from 4000 to $10\ 000\ \text{turns m}^{-1}$. Although the speed is smaller than that of other hygromorph torsional muscles, the torsional stroke is similar or greater than that of graphene hydrogel fiber and multi-ply plasma-treated MWCNT yarn muscle (Table S3, Supporting Information). The rotation

speeds for untwisting and twisting during the actuation cycle were similar, and the ratio of maximum rotation speed for untwist to that for twist was around 0.8 for all the investigated muscles, indicating that desorption of water was almost as fast as absorption of water for the silk muscles.

Figure S18 of the Supporting Information shows the stress dependence of torsional stroke and rotation speed for a 10-cm-long, $\approx 19 \mu\text{m}$ diameter, two-ply, torque-balanced torsional silk muscle driven by water fog. Stress values were calculated by normalizing the applied force to the cross-sectional area of the non-twisted silk filaments before water absorption. The results show that both torsional stroke and maximum rotation speed decreased monotonically with increasing applied stress. This decrease can be explained by the fact that the fiber contracted by $\approx 1\%$ during torsional rotation. From the energy point of view, this behavior can be rationalized from the fact that as we increased the stress, more mechanical energy was consumed by the contractile actuation.

In addition to twist density and applied stress, torsional actuation of the silk muscles is also affected by the pH of the fog, the concentration of the water fog, and the number of fibroin filaments in the plied fiber muscle. Both torsional stroke and rotation speed for a silk fiber muscle reached a maximum when exposed to water fog with pH 7 (Figure S19, Supporting Information), and increased monotonically with increasing water fog concentration (Figure S20, Supporting Information). The maximum torsional stroke and speed were obtained when the fog concentration was $1.1 \text{ g s}^{-1} \text{ m}^{-2}$. However, a higher fog concentration resulted in water condensation on silk surface, which slowed down desorption of water from the silk muscle. Unless otherwise mentioned, the actuation results were obtained using a water fog concentration of $0.22 \text{ g s}^{-1} \text{ m}^{-2}$ with pH 7.

Figure S21 of the Supporting Information shows the relationship between the number of dual-filament silk fibers in a torsional muscle and actuator performance. These silk muscles were prepared (using the process of Figure 2a) from different number of dual-filament silk fibers that had been twisted together using $6000 \text{ turns m}^{-1}$ of twist. When exposed to water fog of $0.22 \text{ g s}^{-1} \text{ m}^{-2}$ at room temperature, the torsional stroke and maximum rotation speed increased and then decreased with increasing the number of silk fibers.

Besides water fog, our silk muscles can also be powered by various solvent vapors, such as acetone, ethanol, and methanol, as shown in Figure S22 of the Supporting Information. We observed a strong correlation between torsional actuation and solvent polarity. High polarity solvent, like water, generated a larger torsional stroke and volume change than for less polar solvents like acetone and ethanol.

In addition to using silk fibroins for artificial muscles, we also investigated other commercial fibers (including cotton, flax, wool, polyester, nylon 6,6, spandex, and so on) so that comparisons could be made for fibers/yarns having nearly the same bias angle. The product of twist density and diameter of the originally twisted fiber was kept constant. Also, the applied stress was held constant. Comparing the performances of torsional muscles produced using different fibers and comparable fabrication conditions, silk muscles provided large torsional stroke ($216^\circ \text{ mm}^{-1}$) and the fastest rotation speed (133 rpm) (Table S4, Supporting Information). The torsional stroke of the tencel ($225^\circ \text{ mm}^{-1}$) was slightly larger than silk, but its rotation

speed was much slower. As long as investigated cycles are sufficient, torsional stroke can be stable and fully reversible for these water-driven commercial fiber muscles. No torsional actuation was observed for polyester, nylon 6, 6, and spandex when exposed to water fog, likely because little absorption of water occurred.

Instead of using plying to make torque-balanced silk muscles, torsional silk muscles can also be made using thermal setting. To prevent untwisting, a two-end-tethered, twisted dual-filament silk fiber was thermally treated in a drying oven at 120°C for 10 min. SEM images of a silk fiber before and after thermal setting show that there was no obvious structural damage after thermal treatment (Figure S23, Supporting Information). X-ray diffraction of a silk fiber before and after thermal setting shows that the main peak associated with β -sheet conformation (around 21° in 2θ for Cu K α) does not significantly shift, indicating that no major structural change resulted from the thermal anneal. However, the intensity of the main peak increased, which indicates an increase in crystallinity of the laterally adjacent ordered regions for the silk fiber after thermal treatment (Figure S24, Supporting Information).^[32] The dependence of mechanical properties of silk fibers on thermal annealing are shown in Figure S25 of the Supporting Information. The fracture strength and the modulus increased 7.4% and 48%, respectively, after annealing, but the failure strain decreased by 1.5%. The enhanced stiffness after thermal setting is consistent with the increase in crystallinity observed by X-ray diffraction.

Thermally set single-ply silk muscles provided reversible, high-stroke torsional actuation in response to humidity change when under isobaric mechanical load (Figure S26, Supporting Information). The investigated 6-cm-long, $\approx 14 \mu\text{m}$ diameter muscle was single-ply and torque balanced (because of thermal setting), and was made from dual-filament silk fiber that had been twisted together using $6000 \text{ turns m}^{-1}$ of twist and then heat-set at 120°C in air for 10 min. Figure S27 of the Supporting Information shows the time dependence of torsional actuation for the above single-ply silk muscle. When ambient RH changed from 20% to 80%, the silk muscle generated a torsional stroke of $157^\circ \text{ mm}^{-1}$. Humidity change was realized by transferring the thermally set silk fiber muscles between two environmental chambers whose humidity was controlled within 1% in a range of 20–90% relative humidity.

The observed torsional actuation for the thermally set single-ply silk muscles can be explained used a single-helix model that was developed for twisted fiber/yarn muscles.^[13,31] When applied to a twisted silk fiber, this model predicts that the relative change in twist is given by

$$\Delta n/n = (\Delta\lambda/\lambda) / \cos^2\alpha_f - \Delta d/d - (\Delta l/l)\tan^2\alpha_f \quad (2)$$

where n is the inserted twist, λ is the length of a helical fiber in the twisted fiber, d is the initial diameter of the twisted fiber before actuation, l is the axial length of the twisted fiber, and Δ indicates changes in these parameters during actuation. According to Equation (2), expansion in the fiber diameter due to absorption of water leads to torsional actuation by yarn untwist. For this application, $\Delta\lambda/\lambda$ and $\Delta l/l$ are relatively small

because of high fiber modulus in their axial directions. The torsional actuation is thus approximated as

$$\Delta T = -T(\Delta d/d) \quad (3)$$

where T is the initially inserted twist n when normalized to initial fiber length before twist insertion and ΔT is the change in T during actuation. This equation predicts that torsional stroke linearly depends on the fiber diameter change resulting from water absorption, as well as the initially inserted fiber twist. As shown in Figure S28 of the Supporting Information, $\Delta d/d$ decreased by only 0.7% as the inserted twist was doubled. Using Equation (3), and these results for the twist dependence of $\Delta d/d$, Figure S29 shows that the predicted torsional strokes, for single-ply muscles having different amount of inserted twists, agreed well with the observed results.

2.4. Fabrication and Performance of Tensile Silk Muscles

Tensile silk muscles were obtained by coiling a twisted two-ply torsional silk muscle on a mandrel and then thermally setting the structure, which is similar to a method previously used for coiled polymer fiber and CNT hybrid yarn muscles.^[10,33] Thermal annealing at 120 °C for 10 min in air was presently used to obtain reversibly actuating mandrel-coiled yarns. Figure 4a schematically illustrates a coiled tensile silk muscle having a plied yarn diameter of d , an outer coil diameter of D , and an intercoil spacing of δ . When the chirality of the individual fiber of the plied silk yarn matches the coil's chirality (homochiral: ZZ or SS), the muscle actuates by contracting during humidity increase. However, when these chiralities are opposite (heterochiral: ZS or SZ), the coiled silk muscle actuates during humidity increase by expanding. The contraction and elongation resulted from untwist of silk fiber during water absorption.

In order to prove that our method of making tensile muscles applies to general textile fibers, we compared tensile performance of fiber muscles made from different commercial fiber materials (Table S5, Supporting Information). Among the textile fibers we researched, all of the tensile muscles could be thermally set. Silk muscle provided large tensile stroke (47%) and fast response rate (0.29% s⁻¹), other humidity-driven muscles also provided fully reversible tensile stroke such as tencel except that no tensile stroke was observed (spandex, nylon 6,6, and so on) when exposed to moisture.

Figure 4b shows that the ZZ and ZS silk muscles provide reversible tensile actuation in response to humidity changes. These results are for muscles made (using the process of Figure 4a) from five parallel silk fibers (each containing two fibroin filaments) that had been twisted together using 6000 turns m⁻¹ of twist, and then folded together (as in Figure 2a). After mandrel coiling and thermal setting, the spring index (D/d) was 7.5, the coil diameter was 1.0 mm, and δ was 1.5 mm and roughly equal to d for ZZ and ZS muscles, respectively.

As shown in Figure 4b, actuator stroke for silk muscles without an applied load increased with increasing humidity and was fully reversible. A contraction of 47% was obtained for the

homochiral muscle and an expansion of 630% resulted for the heterochiral muscle when the humidity increase was from 20% to 80%. Muscle response rate was fast, considering that it was in response to a humidity change (Figures S30 and S31, Supporting Information).

Tensile stroke of silk muscles can be tuned by adjusting the coil index of the spring and the twist inserted into the silk yarn. Figure 4c shows the dependence of tensile stroke on humidity for silk muscles having different twist inserted into the silk yarn. The investigated muscles were made (using the process of Figure 4a) from five parallel silk fibroin filaments, the spring index was 7.5, the coil diameter was 1.0 mm, and δ was 1.5 mm and approximately equal to d for the ZZ and ZS muscles, respectively. Since tensile actuation of a coiled tensile silk muscle was driven by untwisting of the silk yarns during humidity increase, tensile stroke increased monotonically with increasing twist density of the silk yarn and humidity increase (Figure 4c).

Figure 4d shows that tensile stroke increased monotonically with increasing spring coil index for both homochiral and heterochiral silk muscles with yarn twist density of 6000 turns m⁻¹ and without an applied load. For the largest spring index ($C = 22.4$), the maximum stroke for homochiral muscle under no load was 70% within 67 s when actuation was from RH = 20% to RH = 80%, which is much larger than for humidity-driven graphene oxide fiber (5%), CNT/silk fiber (0.4%), and spider silk (0.5%). The silk muscle also showed fast 1.04% s⁻¹ average response rate during contraction, to our knowledge, this is faster than previously reported hygromorph tensile muscles (Table S6, Supporting Information). When the silk muscle was much more tightly coiled ($C = 3.4$), the maximum stroke under no load decreased to 36% for this humidity change. As shown in Figure 4e, both homochiral and heterochiral silk muscles show excellent reversibility during humidity changes from 20% to 60%.

Figure S32 of the Supporting Information shows dependence of tensile stroke on intercoil spacing for a homochiral silk muscle. The investigated muscle was made analogously to the other coiled muscles, using 6000 turns m⁻¹ of twist, a spring index of 7.5, and a coil diameter of 1.0 mm. The maximum tensile stroke was obtained for $\delta = 1.5$.

Tensile stroke for silk muscles decreased monotonically with increasing applied load during humidity changes (20% to 80%) as Figure S33 of the Supporting Information shown. The dependence of work capacity on the applied load is shown in Figure S34 of the Supporting Information. For silk muscle with a spring index of 4.5, work capacity during muscle contraction (i.e., the contractile work capacity) first increased from 0.76 to 1.9 J kg⁻¹ and then decreased to 1.2 J kg⁻¹ with increasing load. Reflecting in part the high coil indices presently deployed, both this contractile work capacity and the ability of the coiled silk muscle to lift weights are very low. However, it should be noted that such a low work capacity is sufficient for its application as smart clothing actually. Large work capacity may require high stiffness, which is not easy to knit and produces uncomfortable feeling for dress.

Previous studies have demonstrated that self-coiled structure obtained by twisting the silk fiber until forming coils is helpful to significantly enhance the work capacities.^[11b] To fully realize

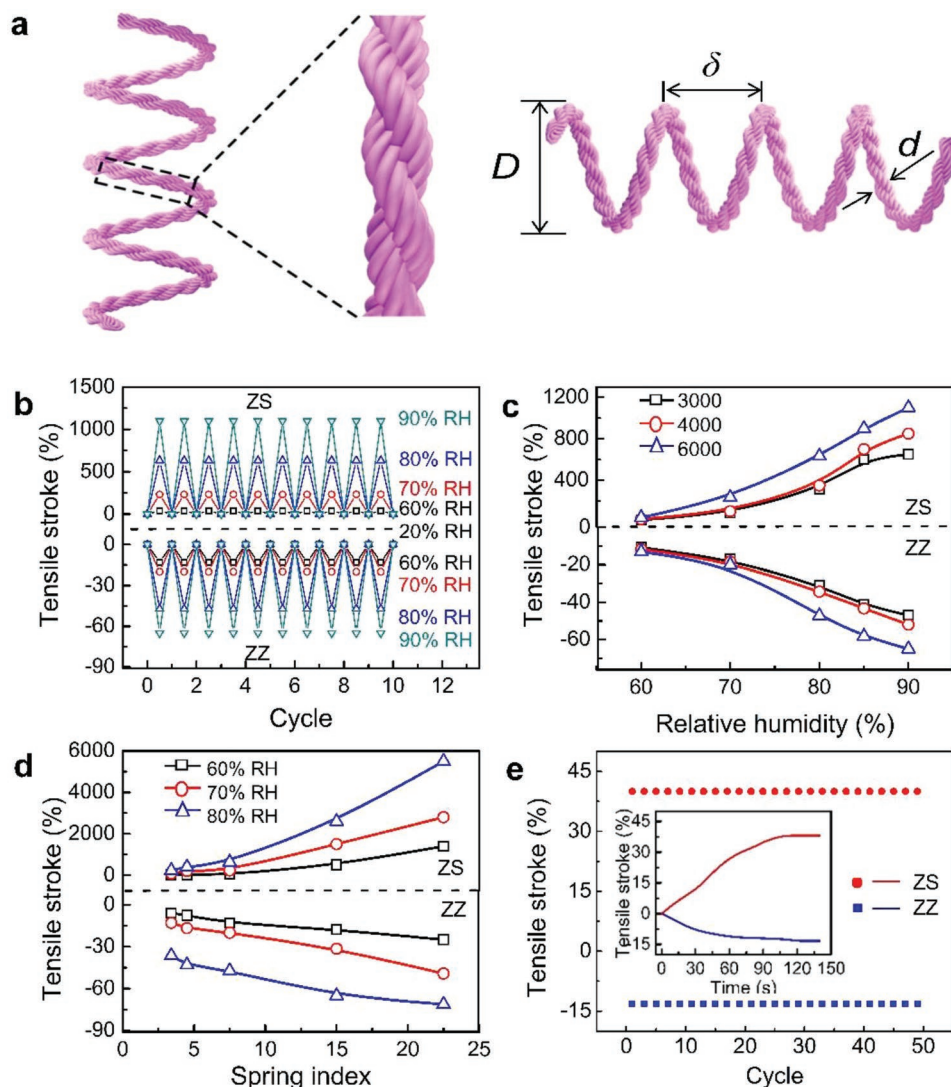


Figure 4. a) Schematic illustration of a coiled tensile silk muscle made from a two-ply torsional silk muscle. b) Tensile stroke change during selected cycles from 20% RH to various other humidities for ZS and ZZ silk muscles. c) Dependence of tensile stroke (relative to muscle length at RH 20%) on relative humidity for tensile silk muscles having different twist densities. d) Dependence of tensile stroke on spring index for ZS and ZZ muscles when humidity was changed from 20% to 60% (black), 70% (red), and 80% (blue). e) Cycling test showing tensile stroke change during humidity change cycles (from 20% to 60%) for ZS (red circles) and ZZ (blue squares) muscles having spring index of 7.5. The inset shows the time dependence of tensile actuation. These silk tensile muscles had a coil diameter of 1.0 mm, and a δ of 1.5 mm and approximately equal to d for the ZZ and ZS silk muscles, respectively, that were made using the process of (a) by first twisting five dual-filament silk fibers together. The spring index for (b), (c), and (e) was 7.5, and the initial twist density for (b), (d), and (e) was $6000 \text{ turns m}^{-1}$.

the potential of work capacities, here, a self-coiled silk yarn with an isobarically applied load was two-end-tethered, the bottom end tether permitted length changes but prevented rotation. By using this configuration, the silk yarn contracted and lifted the load upward once it came into contact with water droplets. For a self-coiled yarn of $262 \mu\text{m}$ in diameter and with a spring index of 1.8 under a stress of 3.2 MPa , a maximum tensile stroke of 3.3% was realized for an optimized load of 12.5 MPa (Figure S35, Supporting Information). The specific work capacity was calculated to be 73 J kg^{-1} , which is ≈ 2 times higher than natural muscle (39 J kg^{-1}). The self-coiled silk yarn provided volumetric energy density of 172 KJ m^{-3} .

2.5. Factors Affecting Torsional and Tensile Actuations

The torsional and tensile actuation can be adjusted by internal parameters of silk muscles and external environmental factors. The internal parameters for torsional muscles include twist density and the number of dual-filament silk fibers. External environmental factors include applied stress, various solvent vapors, solvent polarity, and the concentration of the water fog. The maximum rotation and rotation speed are positively correlated with the concentration of the water fog, and negatively correlated with applied stress. The internal parameters for tensile muscles include chirality, twist density, spring index, and intercoil spacing.

The external environmental factor investigated is humidity. Homochiral muscle actuates by contracting during humidity increase, while the heterochiral muscle actuates during humidity increase by expanding. With the increase of twist density, spring index, or humidity tensile stroke increases monotonically.

2.6. Applications of Silk Muscles

The demonstrated reversible torsional and tensile silk muscles open up the door for a variety of promising applications. **Figure 5a** shows that a crawling robotic “caterpillar” made of a coiled silk muscle on a barbed wire. The robotic caterpillar was made (using the process of Figure 4a) from five dual-filament silk fibers that had been twisted together using 6000 turns m^{-1} of twist, having a spring index of 7.5 and coil diameter of 1 mm. Since the barb pins on the wire incline in one direction, when humidity changes using water vapor from finger sweat, caterpillar expanded and contracted so that the “caterpillar” moved in one direction (Movie S1, Supporting Information).

Silk textile provides excellent comfort and drapability. Here, we demonstrate a smart textile woven from silk fiber muscles, which responds to humidity change in the environment.

The coiled tensile silk muscles were made (using the process of Figure 4a) from 30 dual-filament silk fibers that had been twisted together using 2500 turns m^{-1} of twist, having a spring index of 1.1 and coil diameter of 0.5 mm. The sleeves of the smart textile was made by weaving coiled silk muscle fibers in the warp direction and untwisted fibers in the weft direction (Figure 5b). In the textile industry, the warp density of clothing fabrics is usually 21–128 yarn counts per inch. In our experiment, the warp density of smart clothing was up to 40 yarn counts per inch (Figure 5b), which can be tuned into diverse denseness for actual textile industry by adjusting the distance between silk muscles, spring index, thickness of silk yarns or knitting method. As shown in Figure 5c, the sleeves of the smart textile shrink in the warp (vertical) direction when humidity increases (for example, due to perspiration or humid environment), and then expands when humidity decreases. The investigated smart sleeves generated a large contraction (45%) when exposed to moisture or sweat, and then recovered to its initial length when the environment became dry (Figure 5c; Movie S2, Supporting Information). This moisture-responsive textile, which can change macroshape or microstructure, is promising to be very effective to achieve such functions for moisture and thermal management for increased comfort between skin and fabric (Figure 5d; Movie S3, Supporting Information).



Figure 5. a) Sequential photos showing a robotic “caterpillar” walking on a barbed wire, which was driven by moisture from a finger. b) Photographs of smart textile woven from tensile silk muscles, which had different weavings. One tensile silk muscle was made from twisting 30 dual-filament silk fibers. c) Sequential photos showing sleeves of smart clothing contracted when exposed to moisture and recovered to its original length when exposed to dry air. d) Sequential photos showing smart clothing can change macroshape or microstructure to achieve moisture and thermal management.

Additionally, silk can also be combined with carbon nanotubes or graphene to obtain composite fibers which have multiple functions such as electrical conductive, sensing, and actuation.^[34] Such functions endow them with great potential for a variety of applications including wearable sensors, electronic skin, and human–machine interfaces.

3. Conclusion

In summary, we have demonstrated high-performance water fog and humidity-driven torsional and tensile silk artificial muscles using degummed silk fibers and studied the detailed mechanisms using molecular dynamics simulation. Our torsional silk muscles provided a fully reversible torsional stroke of $547^\circ \text{ mm}^{-1}$ when exposed to water fog, which was close to the reported torsional stroke for a moisture-driven twisted graphene fiber ($588.6^\circ \text{ mm}^{-1}$),^[10b] and nine times that of a water-absorption-driven coiled carbon-nanotube fiber ($61.3^\circ \text{ mm}^{-1}$).^[11b] Coiled tensile silk muscles provided a 70% contraction when the RH changed from 20% to 80%, which was larger than for a coiled CNT yarn muscle driven by organic solvents (60%).^[25] The peak work capacity was up to 73 J kg^{-1} . Molecular dynamics simulation showed that water absorption resulted in loss of hydrogen bonds within the silk proteins, which further led to structural transformations that provides the basic mechanism for activation. We also demonstrated smart walking robot (caterpillar), and moisture-sensitive smart textile using our silk muscles. Because silk is largely abundant and cost-effective, our silk muscles will open the path to more possibility in diverse applications, such as smart textiles and soft robotics.

4. Experimental Section

Preparation of Silk Muscles: *Bombyx mori* (silkworm) cocoon was purchased from Lihua Co. Ltd, China. The raw silk fiber was obtained by using a standard reeling method. First, the cocoon was completely immersed in hot water of 90°C for 15 min, and then it was moved from the hot water to double-distilled water at 40°C for reeling. Raw silk fibers were obtained through reeling using a reeling speed of $\approx 5 \text{ cm s}^{-1}$. Afterward the raw silk fibers were soaked in an aqueous solution of NaOH (0.19 mol L^{-1}) or H_2SO_4 (0.1 mol L^{-1}) for 24 h at room temperature, rinsed thoroughly with DI water, and dried at room temperature.

The obtained dual-filament silk fibers were used for fabricating the twisted silk yarns. Briefly, one end of silk fiber was fixed to the tip of an electric motor, and the other end was loaded with a clip weighing 50.0 mg. The entire silk fiber was suspended between the motor and the clip, and twist was inserted. During twist insertion, the fiber was continuously shortened. Torsional silk muscles were obtained by folding a twisted single dual-filament fiber or a twisted multiple dual-filament fibers onto itself (by bending at fiber midpoint), which results in fiber plying. Tensile silk muscles were obtained by coiling a two-ply torsional silk muscle on a mandrel and then thermally setting the structure. For thermal setting, a torsional silk muscle was wrapped around a steel bar to form a coil with two ends fixed using polyimide adhesive tape. The condition for thermal setting was 120°C for 10 min in an oven.

Characterizations: The mechanical properties of twisted and nontwisted silk fibers were measured using an Instron mechanical tester (model 3365). To obtain the cross-sectional area of the samples,

silk fiber diameter was measured using SEM. For mechanical testing, samples were attached to paper frames using double-sided adhesive tape. The gauge length was 30.0 mm. The frames were mounted onto the Instron tester equipped with a calibrated 5 N load cell. The extension rate was 5.0 mm min^{-1} . SEM characterization was carried out using an FEI Quanta microscope (QUANTA 200). FTIR spectroscopy was carried out on a TENSOR 37 FTIR spectrometer. Thermal degradation of silk fibers was measured using thermogravimetric analysis on a Thermogravimetry (model NETZSCH TG209) from 20 to 650°C in N_2 at a scanning speed of $10^\circ \text{C min}^{-1}$. The X-ray diffraction results were obtained using $\text{Cu K}\alpha$ radiation on an Ultima IV X-ray diffractometer. The data were collected from 5° to 40° . The 2D X-ray diffraction patterns were obtained using MicroMax 007 HF on a Rigaku X-ray diffractometer (BioSAXS-2000). Ambient temperature and relative humidity were measured by a hygrometer (CEM DT-615).

Molecular Dynamics Simulation of Bombyx Mori Silk Fibroin: Molecular simulations of *bombyx mori* silk fibroin were conducted using GROMACS with Amber 03 force field. The initial structures were constructed based on the models obtained from Protein Data Bank Entry (PID: 3PUB/2FJY/3UA0). The three models were solvated in three simulation boxes with the dimensions of $1.4 \times 1.4 \times 1.4 \text{ nm}^3$, $1.1 \times 1.1 \times 1.1 \text{ nm}^3$, and $1.0 \times 1.0 \times 1.0 \text{ nm}^3$, respectively to mimic the fully hydrated environment. The hydrated systems were further subjected to the energy minimization (EM), equilibration of NVT at 300 K followed by NPT at pressure of 1 bar. Finally, the systems were relaxed by running production molecular simulations (MD) with periodic boundary condition and Particle Mesh Ewald for long-range electrostatic interactions. After 30 ns equilibrium process, systems reached to the final equilibration where all parameters, including interaction energy, hydrogen bond, and gyration radius were fully converged. In order to investigate the effect of water on the system, MD simulations of the three proteins in the vacuum (without water) were also conducted with the similar processes of EM, NVT, NPT, and MD. Visualized molecular dynamics (VMD) was utilized for capturing the snapshots to illustrate the configuration change. To quantitatively analyze the simulation results, the hydrogen bond, interaction energy, and gyration radius were calculated via GROMACS and the proportion of secondary structure in the whole system was obtained from VMD.

Supporting Information

Supporting Information is available from the Wiley Online Library or from the author.

Acknowledgements

This work was supported by the Science Foundation for Distinguished Young Scholars of Tianjin (Grant No. 18JCQJC46600), the National Key Research and Development Program of China (2017YFB0307000), the National Natural Science Foundation of China (Grant Nos. U153122 and 51773094), the Natural Science Foundation of Tianjin (Grant No. 18JCZDJC36800), the Fundamental Research Funds for the Central Universities (63171219), the Science and Technology Support Program of Changzhou (CZ20170007), the State Key Laboratory for Modification of Chemical Fibers and Polymer Materials, Donghua University (LK1704), China Postdoctoral Science Foundation Funded Project (Grant No. 2017M620752), and the National Science Foundation (Grant No. CMMI 1727960).

Conflict of Interest

The authors declare no conflict of interest.

Keywords

silk fiber, smart textile, soft robot, tensile muscle, torsional muscle

Received: November 20, 2018

Revised: February 20, 2019

Published online:

- [1] Report: Smart Textiles Are Fashion's Fourth Industrial Revolution, <https://apparelmag.com/report-smart-textiles-are-fashions-fourth-industrial-revolution> (accessed: September 2016).
- [2] Z. Wen, M.-H. Yeh, H. Guo, J. Wang, Y. Zi, W. Xu, J. Deng, L. Zhu, X. Wang, C. Hu, *Sci. Adv.* **2016**, 2, e1600097.
- [3] S. H. Kim, C. S. Haines, N. Li, K. J. Kim, T. J. Mun, C. Choi, J. Di, Y. J. Oh, J. P. Oviedo, J. Bykova, S. Fang, N. Jiang, Z. Liu, R. Wang, P. Kumar, R. Qiao, S. Priya, K. Cho, M. Kim, M. S. Lucas, L. F. Drummy, B. Maruyama, D. Y. Lee, X. Lepro, E. Gao, D. Albarq, R. Ovalle-Robles, S. J. Kim, R. H. Baughman, *Science* **2017**, 357, 773.
- [4] a) I. Das, G. De, *Sci. Rep.* **2016**, 5, 18503; b) K. Qi, X. Chen, Y. Liu, J. H. Xin, C. Mak, W. A. Daoud, *J. Mater. Chem.* **2007**, 17, 3504.
- [5] T. Yamada, Y. Hayamizu, Y. Yamamoto, Y. Yomogida, A. Izadi-Najafabadi, D. N. Futaba, K. Hata, *Nat. Nanotechnol.* **2011**, 6, 296.
- [6] A. Laforgue, G. Rouget, S. Dubost, M. F. Champagne, L. Robitaille, *ACS Appl. Mater. Interfaces* **2012**, 4, 3163.
- [7] Z. Zhang, K. Guo, Y. Li, X. Li, G. Guan, H. Li, Y. Luo, F. Zhao, Q. Zhang, B. Wei, Q. Pei, H. Peng, *Nat. Photonics* **2015**, 9, 233.
- [8] P.-C. Hsu, C. Liu, A. Y. Song, Z. Zhang, Y. Peng, J. Xie, K. Liu, C.-L. Wu, P. B. Catrysse, L. Cai, S. Zhai, A. Majumdar, S. Fan, Y. Cui, *Sci. Adv.* **2017**, 3, e1700895.
- [9] Y. Zhong, F. Zhang, M. Wang, C. J. Gardner, G. Kim, Y. Liu, J. Leng, S. Jin, R. Chen, *Sci. Rep.* **2017**, 7, 44208.
- [10] P. Chen, Y. Xu, S. He, X. Sun, S. Pan, J. Deng, D. Chen, H. Peng, *Nat. Nanotechnol.* **2015**, 10, 1077.
- [11] a) H. Cheng, Y. Hu, F. Zhao, Z. Dong, Y. Wang, N. Chen, Z. Zhang, L. Qu, *Adv. Mater.* **2014**, 26, 2909; b) M. D. Lima, N. Li, M. Jung de Andrade, S. Fang, J. Oh, G. M. Spinks, M. E. Kozlov, C. S. Haines, D. Suh, J. Foroughi, S. J. Kim, Y. Chen, T. Ware, M. K. Shin, L. D. Machado, A. F. Fonseca, J. D. W. Madden, W. E. Voit, D. S. Galvão, R. H. Baughman, *Science* **2012**, 338, 928; c) J. Di, S. Fang, F. A. Moura, D. S. Galvão, J. Bykova, A. Aliev, M. Jung de Andrade, X. Lepro, N. Li, C. Haines, R. Ovalle-Robles, D. Qian, R. H. Baughman, *Adv. Mater.* **2016**, 28, 6598.
- [12] a) W.-Y. Wu, J.-Y. Lee, *Text. Res. J.* **1995**, 65, 522; b) M. Miao, R. Chen, *Text. Res. J.* **1993**, 63, 150.
- [13] C. S. Haines, M. D. Lima, N. Li, G. M. Spinks, J. Foroughi, J. D. W. Madden, S. H. Kim, S. Fang, M. Jung de Andrade, F. Göktepe, Ö. Göktepe, S. M. Mirvakili, S. Naficy, X. Lepro, J. Oh, M. E. Kozlov, S. J. Kim, X. Xu, B. J. Swedlove, G. G. Wallace, R. H. Baughman, *Science* **2014**, 343, 868.
- [14] S. Ling, Z. Qin, C. Li, W. Huang, D. L. Kaplan, M. J. Buehler, *Nat. Commun.* **2017**, 8, 1387.
- [15] a) S. Wang, T. Li, C. Chen, W. Kong, S. Zhu, J. Dai, A. J. Diaz, E. Hitz, S. D. Solares, T. Li, L. Hu, *Adv. Funct. Mater.* **2018**, 28, 1707491; b) C. Jia, C. Chen, Y. Kuang, K. Fu, Y. Wang, Y. Yao, S. Kronthal, E. Hitz, J. Song, F. Xu, B. Liu, L. Hu, *Adv. Mater.* **2018**, 30, 1801347; c) K. Zhu, C. Qiu, A. Lu, L. Luo, J. Guo, H. Cong, F. Chen, X. Liu, X. Zhang, H. Wang, *ACS Sustainable Chem. Eng.* **2018**, 6, 5314.
- [16] N. Padaki, B. Das, A. Basu, *Advances in Silk Science and Technology*, Elsevier, Woodhead, UK **2015**.
- [17] Z. Shao, F. Vollrath, *Nature* **2002**, 418, 741.
- [18] G. S. Perrone, G. G. Leisk, T. J. Lo, J. E. Moreau, D. S. Haas, B. J. Papenburg, E. B. Golden, B. P. Partlow, S. E. Fox, A. M. S. Ibrahim, S. J. Lin, D. L. Kaplan, *Nat. Commun.* **2014**, 5, 3385.
- [19] M. L. Gulrajani, *Rev. Prog. Color. Relat. Top.* **1992**, 22, 79.
- [20] K. Kanehisa, *U.S. Patent No. 5849040*, **1998**.
- [21] W. Zuwang, *Rev. Prog. Color. Relat. Top.* **1998**, 28, 32.
- [22] S. He, P. Chen, L. Qiu, B. Wang, X. Sun, Y. Xu, H. Peng, *Angew. Chem.* **2015**, 127, 15093.
- [23] J. Deng, Y. Xu, S. He, P. Chen, L. Bao, Y. Hu, B. Wang, X. Sun, H. Peng, *Nat. Protoc.* **2017**, 12, 1349.
- [24] F. Happey, A. J. Hyde, *Nature* **1952**, 169, 921.
- [25] Y. Takahashi, *Silk Polymers: Materials Science and Biotechnology*, ACS, Washington, DC **1994**.
- [26] a) Z. Zhu, D. Gong, L. Liu, Y. Wang, *Anal. Bioanal. Chem.* **2014**, 406, 2709; b) R. M. Robson, *Int. J. Biol. Macromol.* **1999**, 24, 145.
- [27] a) K. Yazawa, K. Ishida, H. Masunaga, T. Hikima, K. Numata, *Biomacromolecules* **2016**, 17, 1057; b) A. Nishimura, H. Matsuda, Y. Tasei, T. Asakura, *Biomacromolecules* **2018**, 19, 563; c) C. Mo, P. Wu, X. Chen, Z. Shao, *Vib. Spectrosc.* **2009**, 51, 105; d) G. Chen, N. Matsuhisa, Z. Liu, D. Qi, P. Cai, Y. Jiang, C. Wan, Y. Cui, W. R. Leow, Z. Liu, S. Gong, K.-Q. Zhang, Y. Cheng, X. Chen, *Adv. Mater.* **2018**, 30, 1800129.
- [28] A. Nova, S. Keten, N. M. Pugno, A. Redaelli, M. J. Buehler, *Nano Lett.* **2010**, 10, 2626.
- [29] M. K. Lima-Tenório, E. T. Tenório-Neto, M. R. Guilherme, F. P. Garcia, C. V. Nakamura, E. A. G. Pineda, A. F. Rubira, *Chem. Eng. J.* **2015**, 259, 620.
- [30] N. L. Thomas, A. H. Windle, *Polymer* **1982**, 23, 529.
- [31] J. Foroughi, G. M. Spinks, G. G. Wallace, J. Oh, M. E. Kozlov, S. Fang, T. Mirfakhrai, J. D. W. Madden, M. K. Shin, S. J. Kim, R. H. Baughman, *Science* **2011**, 334, 494.
- [32] a) M. Tsukada, G. Freddi, M. Nagura, H. Ishikawa, N. Kasai, *J. Appl. Polym. Sci.* **1992**, 46, 1945; b) H. Kweon, S. O. Woo, Y. H. Park, *J. Appl. Polym. Sci.* **2001**, 81, 2271; c) J. Magoshi, M. Mizuide, Y. Magoshi, K. Takahashi, M. Kubo, S. Nakamura, *J. Polym. Sci., Part B: Polym. Phys.* **1979**, 17, 515.
- [33] X. Gu, Q. Fan, F. Yang, L. Cai, N. Zhang, W. Zhou, W. Zhou, S. Xie, *Nanoscale* **2016**, 8, 17881.
- [34] a) Q. Wang, M. Jian, C. Wang, Y. Zhang, *Adv. Funct. Mater.* **2017**, 27, 1605657; b) Z. Yin, M. Jian, C. Wang, K. Xia, Z. Liu, Q. Wang, M. Zhang, H. Wang, X. Liang, X. Liang, Y. Long, X. Yu, Y. Zhang, *Nano Lett.* **2018**, 18, 7085.

ADVANCED FUNCTIONAL MATERIALS

Supporting Information

for *Adv. Funct. Mater.*, DOI: 10.1002/adfm.201808241

Moisture Sensitive Smart Yarns and Textiles from Self-Balanced Silk Fiber Muscles

*Tianjiao Jia, Yang Wang, Yuanyuan Dou, Yaowang Li, Monica Jung de Andrade, Run Wang, Shaoli Fang, Jingjing Li, Zhou Yu, Rui Qiao, Zhuangjian Liu, Yuan Cheng, Yewang Su, Majid Minary-Jolandan, Ray H. Baughman, Dong Qian, and Zunfeng Liu**

Supplementary Information for

Moisture Sensitive Smart Yarns and Textiles from Self-Balanced Silk Muscles

*Tianjiao Jia, Yang Wang, Yuanyuan Dou, Yaowang Li, Monica Jung de Andrade, Run Wang, Shaoli Fang, Jingjing Li, Zhou Yu, Rui Qiao, Zhuangjian Liu, Yuan Cheng, Yewang Su, Majid Minary-Jolandan, Ray H. Baughman, Dong Qian, and Zunfeng Liu**

*Corresponding author: Zunfeng Liu

Email: liuzunfeng@nankai.edu.cn (Z.L.)

This PDF file includes:

Supporting Text
Figures S1 to S35
Tables S1 to S6
Captions for movies S1 to S3
References for SI reference citations

Other supplementary materials for this manuscript include the following:

Movies S1 to S3

Structural analysis of degummed silk

The Fourier transform infrared (FTIR) spectra (Figure S3) of the non-treated, H₂SO₄-degummed, and NaOH-degummed fibers were quite similar, and showed the expected chemical bonds and molecular conformation of silk proteins. The fibroin exists as β -sheet with crystallized conformation, while the sericin exists in random coil form with an amorphous structure,^[1] which enables structural assignments. The α -helices, anti-parallel and parallel β -sheets, and random coil structures are indicated by the frequencies of the amide band. The amide I mode at 1615-1640 cm⁻¹ reflects the β -sheet conformation, and the amide II band in the range of 1640-1660 cm⁻¹ is associated with the random coil and α -helix conformations. For all samples, the peak at 1235 cm⁻¹ in the amide III band, which is related to random coil conformation and helical conformation, was clearly seen, while the peak at 1260 cm⁻¹, which is due to the β -sheet conformation, was very weak. The absorption peak centered at 1700 cm⁻¹ was classified as a β -turn.^[2] The IR absorption peak at 1515 cm⁻¹ in the amide II band, which is attributed to N-H deformations of a β -sheet conformation,^[2b] had the highest relative intensity in the silk degummed using NaOH. Silk fibers untreated and degummed with H₂SO₄ and NaOH exhibited strong IR peaks at 1650 cm⁻¹, 1515 cm⁻¹, and 1230 cm⁻¹. However, the IR shoulder peaks at 1260 cm⁻¹ and 1700 cm⁻¹ had higher relative intensities in the silk degummed by NaOH. This is consistent with the higher crystalline component in the silk degummed by NaOH, because of reduction in the content of the amorphous sericin.

The X-ray diffraction patterns of untreated and degummed silk samples had the same peak positions and peak intensities (Figure S4). There was a main peak at about 21° (0.934 nm), which is attributed to the β -sheet conformation, and two shoulder peaks at about 11° (0.428 nm) and 24° (0.358 nm), which are due to the α -helix and β -sheet conformations, respectively.^[3] This absence of diffraction pattern change upon removal of the sericin is expected because the sericin is largely amorphous.

Degumming did not significantly affect the thermal stability of the silk fibers (Figure S5). Importantly, for actuator applications, the force-displacement curves of Figure S6a show that reduction of silk fiber diameter by sericin removal did not dramatically decrease the rupture force or the initial force constant for elastic deformation. Moreover, the stress-strain curves of Figure S6b show that reduction in sericin content by degumming increased fiber fracture stress and slightly decreased the failure strain.

Calculation details

The helical bias angle (α) of a silk fiber can be calculated from the following equation:^[4]

$$\tan \alpha = \pi d T \quad (\text{S1})$$

where d represents the silk fiber diameter (in meters), and T is the inserted twist density of the fiber (in turns m⁻¹). The silk fiber diameter (d) and the helical angle (α) were obtained from scanning electron microscopy (SEM) measurements. The

cross-section of silk was approximated as an ellipse, so the average of the long axis and the short axis were used for calculation of the silk diameter (d).^[1, 5] For torsional muscle characterization, the paddle's rotation was recorded using a high-speed camera. The paddle was considered as a semicircular ring, R is the outer radius, and R_0 is the inner radius of the semicircular ring. The R and R_0 were measured as 1.95 mm and 1.00 mm, respectively. In the torsional actuation experiments, the moment of inertia (I) of the paddle having a weight (M) of 50.0 mg is calculated as

$$I = M(R^2 + R_0^2)/4 \quad (\text{S2})$$

and therefore the maximum torque (τ) is calculated as

$$\tau = Ia \quad (\text{S3})$$

The mass (m) of the silk muscle before actuation was 45.8 μg . Therefore the specific torque (τ_s) with respect to the mass of the silk muscle is calculated as

$$\tau_s = \tau/m \quad (\text{S4})$$

For the tensile actuation, the initial length of the silk muscle is L_0 , and the coil length after contraction or expansion is L , then the tensile stroke is calculated as

$$\text{Tensile stroke (\%)} = (L - L_0)/L_0 \times 100\% \quad (\text{S5})$$

The work capacity per mass of the silk muscle (W) was calculated by dividing the work of contraction (in Joule) by the mass (in kg) of the silk muscle. The equation used for this calculation is

$$W = Mg\Delta H/m \quad (\text{S6})$$

where M is the isobaric load, g is gravitational acceleration, and ΔH is the change of height.

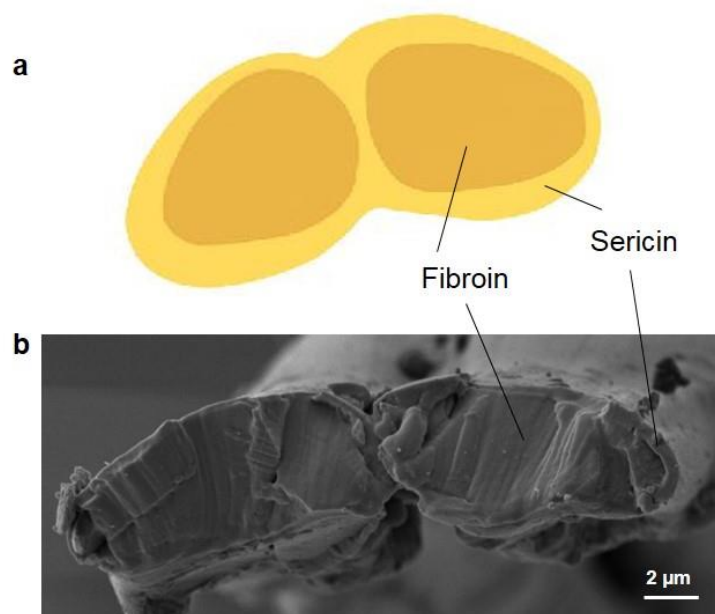


Figure S1. Schematic illustration (a) and SEM image (b) of the cross-section of a raw silk fiber, which shows a core-shell structure.

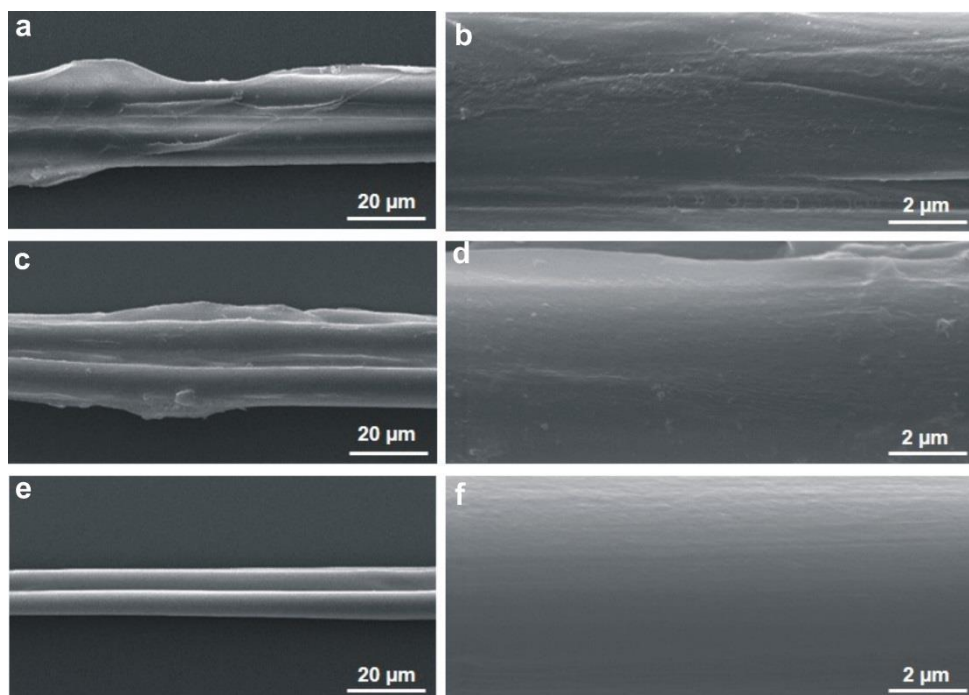


Figure S2. Low and high magnification SEM images of silk fibers that are untreated (a, b), degummed using sulfuric acid solution (c, d) and degummed using NaOH solution (e, f).

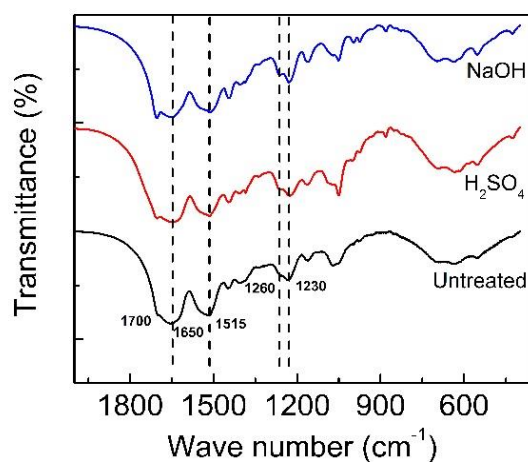


Figure S3. FTIR spectra of silkworm silks that are untreated, degummed using NaOH solution, and degummed using H₂SO₄ solution. The experiments were conducted under ambient conditions at RH of ~10% at 25 °C.

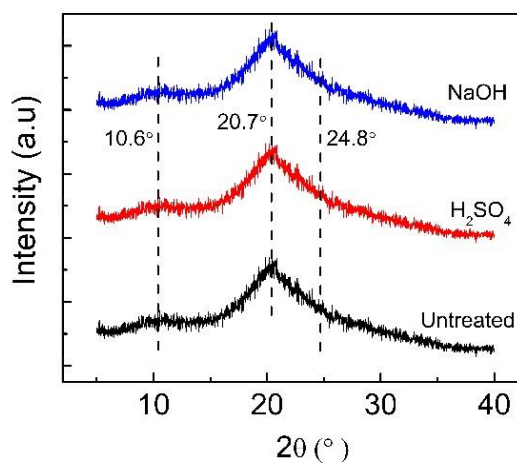


Figure S4. X-ray diffraction patterns (CuK α radiation) of silkworm silks that are untreated, degummed using NaOH solution, and degummed using H₂SO₄ solution. The results indicated the crystalline structure of the silk fibroin fiber was not significantly affected by the degumming process. The experiments were conducted under ambient conditions at RH of ~30% at 25 °C.

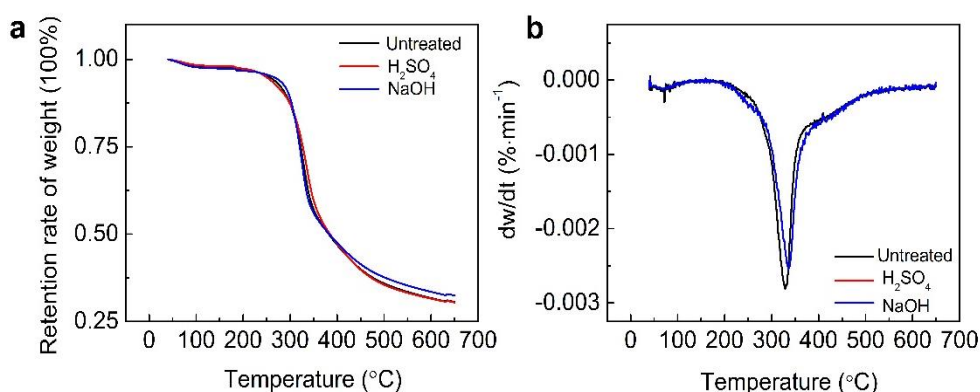


Figure S5. Thermal gravimetric (TG) analysis scans (a) and differential thermal gravimetric (DTG) plots (b) of silkworm silks that are untreated, degummed using NaOH solution, and degummed using H₂SO₄ solution. The samples were in flowing N₂ during the measurements.

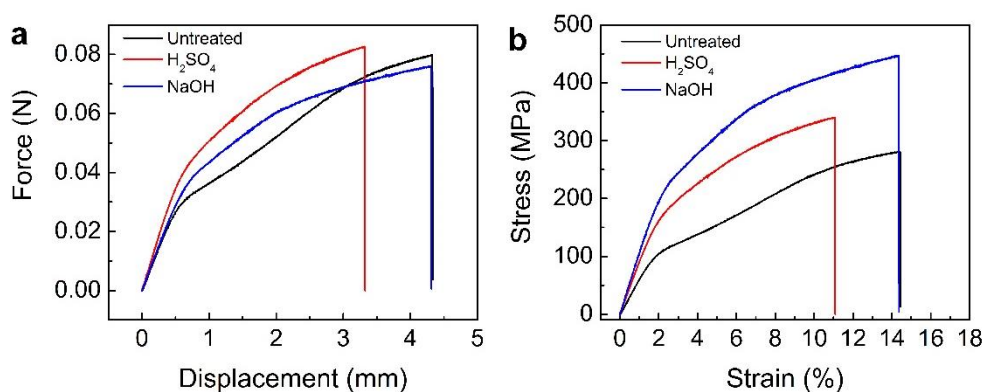


Figure S6. Force-displacement curves (a) and engineering stress-strain curves (b) of silkworm fiber that is untreated, degummed using NaOH solution, and degummed using H₂SO₄ solution. The experiments were conducted under ambient conditions at RH of ~30% at 25 °C.

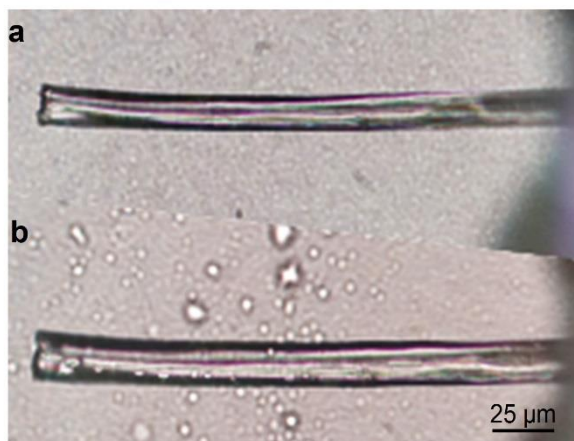


Figure S7. Photographs of a degummed silk fiber (taken using an OLYMPUS BX53 metalloscope) before (a) and after (b) absorption of water fog at room temperature. The fiber diameter increases by about 15% because of this water absorption. Degumming was by treatment with NaOH solution.

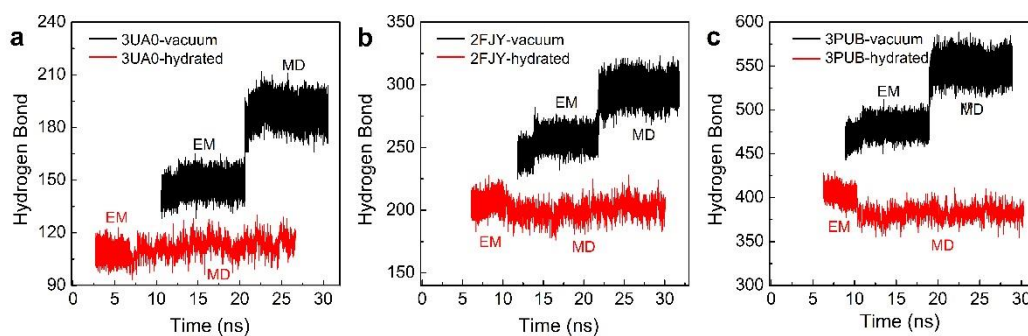


Figure S8. Simulation results showing the effects of water on the history of hydrogen bond. The black curve represents the model without water and the red curve is for the hydrated model. EM and MD are abbreviations of energy minimization and molecular dynamics, respectively, in Figures S8-S10.

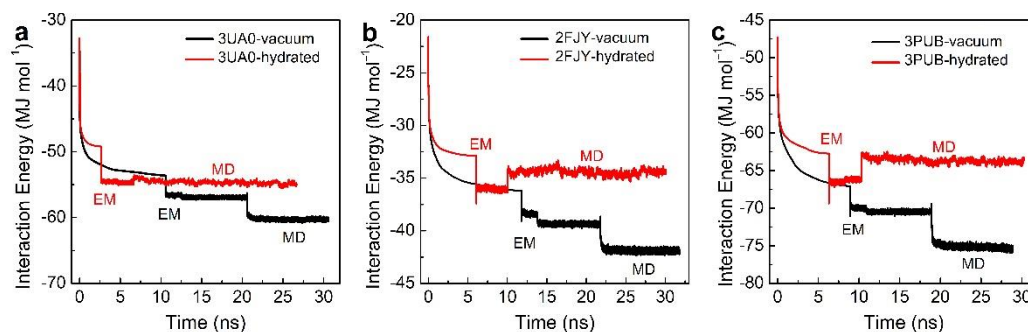


Figure S9. Simulation results showing the effects of water on the history of interaction energy. The black curve represents the model without water and the red curve is for the hydrated model.

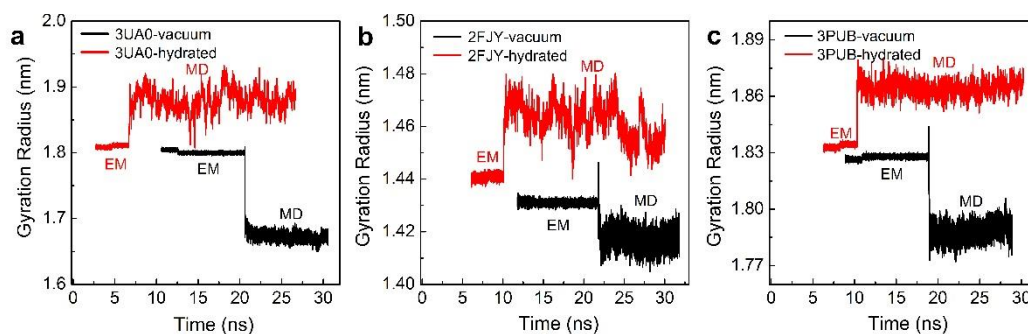


Figure S10. Simulation results showing the effects of water on the history of gyration radius. The black curve represents the model without water and the red curve is for the hydrated model.

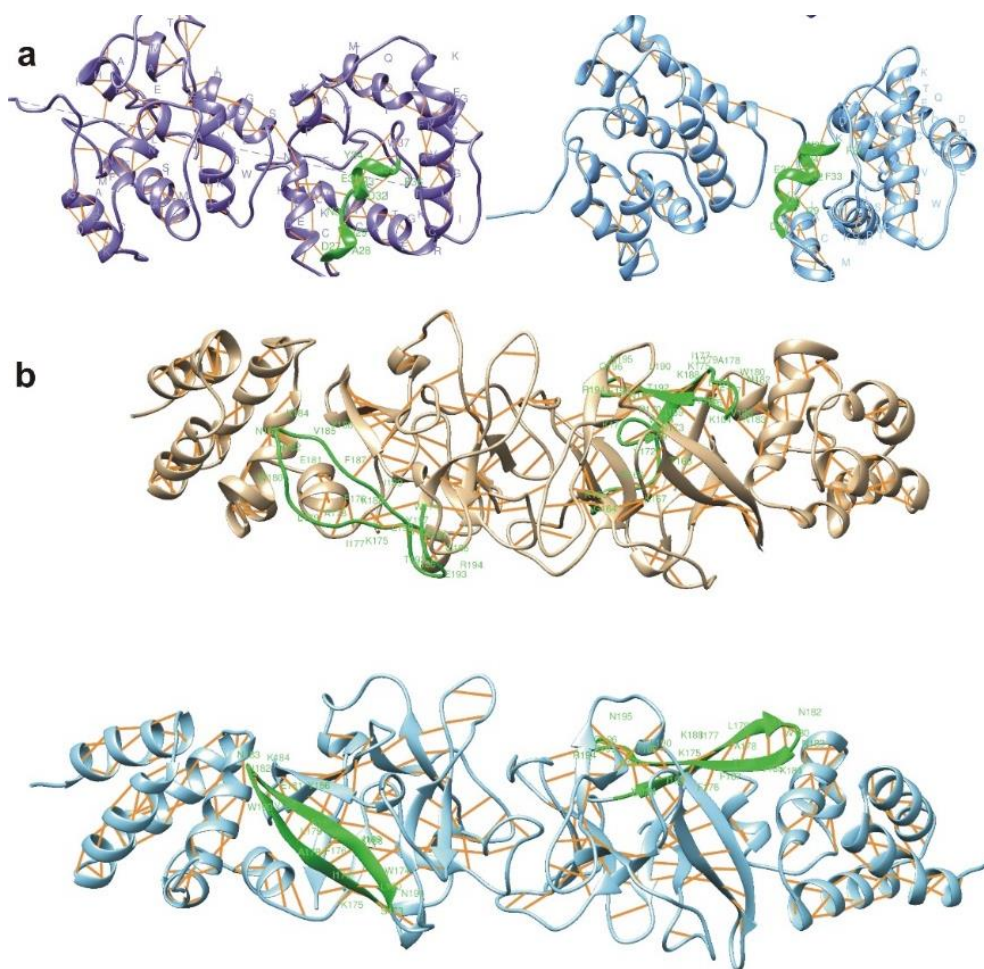


Figure S11. Molecular dynamic simulation of the proteins (pdb IDs are 2FJY and 3PUB) before and after water molecules added. The green parts of protein 2FJY shows the length of helix became longer in a way that two short helices and part of loops merged into a new longer helix (a). The green parts of protein 3PUB illustrate that the loop structures formed new beta-strands or merged into a longer strand (b).

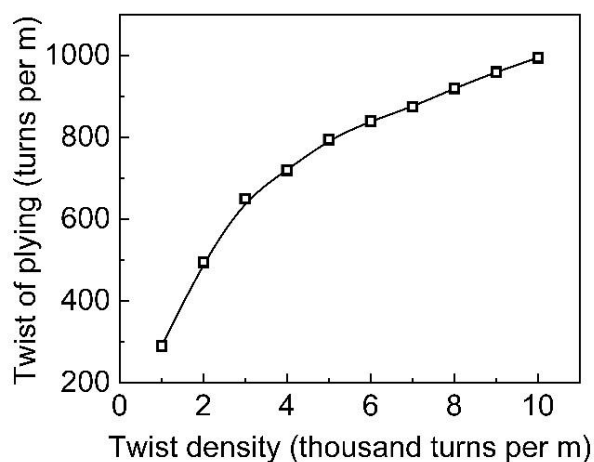


Figure S12. Twist of plying as a function of the twist density of the initial silk yarn, where the plying results under an applied load to provide a torque-balance structure for the folded yarn. The experiments were conducted under ambient conditions at RH of ~20% and 25 °C. (The length of the silk fiber before twisting was 20.0 cm and the isobaric load applied to the folded yarn (illustrated in Figure 2a) was 480.0 mg.

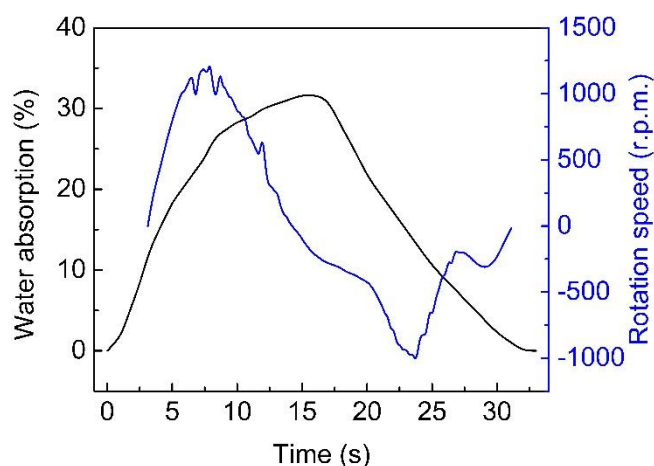


Figure S13. Time dependence of rotation speed and water absorption during a rotation cycle. The investigated torsional silk muscles were made (using the process of Figure 2a) from a single dual-filament silk fiber that was two-ply and torque balanced. The length of the silk muscle was 10.0 cm, the isobaric load was 50.0 mg, and the initial inserted twist density was 9000 turns m^{-1} .

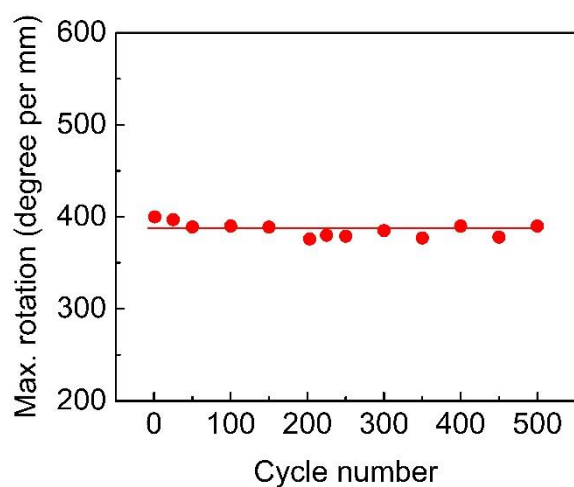


Figure S14. Cycling test showing the change of maximum rotation during actuation cycles in which the torsional silk muscle was exposed to ultrasonically generated fog and then delivery of the fog was interrupted.

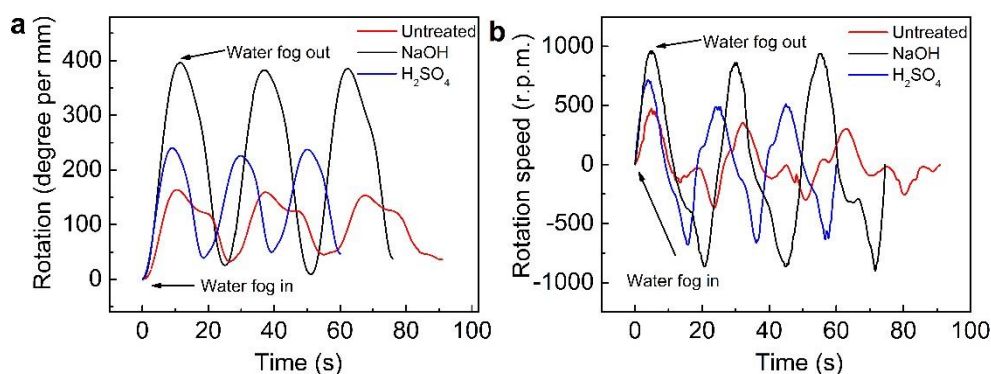


Figure S15. Torsional actuation (a) and rotation speed (b) as a function of time for torsional silk muscles that are untreated, degummed using NaOH solution, and degummed using H₂SO₄ solution. Actuation was driven by switching water fog (0.22 g s⁻¹ m⁻²) on and off for three cycles. The investigated torsional silk muscles were made (using the process of Figure 2a) from a single dual-filament silk fiber that was two-ply and torque balanced. The length of the silk muscle was 10.0 cm, the isobaric load was 50.0 mg, and the initial inserted twist density was 9000 turns m⁻¹.

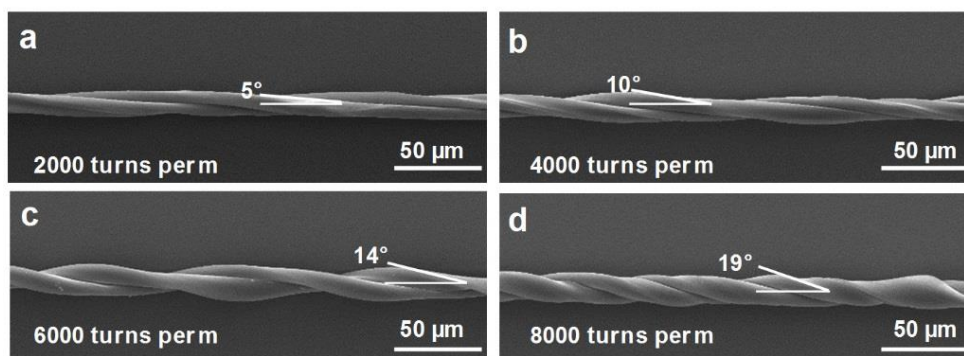


Figure S16. SEM images of two-ply silk fiber having twist densities of (a), 2000; (b), 4000; (c), 6000; and (d), 8000 turns m^{-1} .

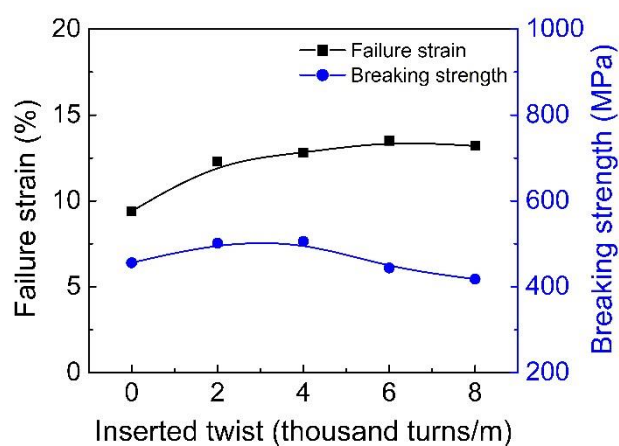


Figure S17. Dependence of failure strain and breaking strength of a two-ply silk fiber on the amount of twist inserted for plying under ambient conditions of ~10% RH at 25 °C.

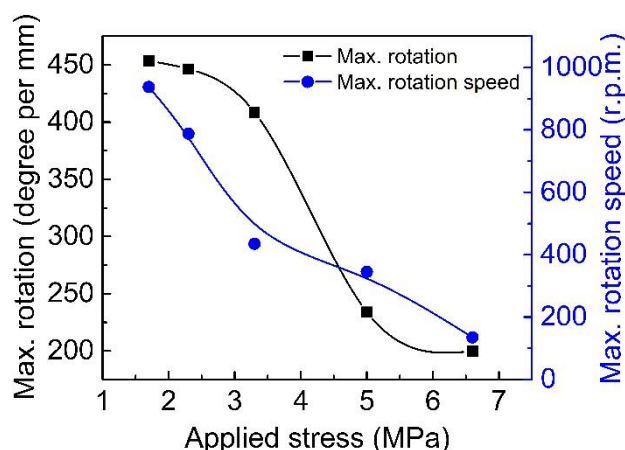


Figure S18. The dependence of the torsional stroke and maximum rotation speed for a silk fiber muscle on the applied stress driven by water fog of $0.22 \text{ g s}^{-1} \text{ m}^{-2}$. The investigated torsional silk muscle (10 cm long and $19\text{-}\mu\text{m}$ in diameter) was made (using the process of Figure 2a) from a single alkali-degummed dual-filament silk fiber that was two-ply and torque balanced. The isobaric load was 50.0 mg, and the initial inserted twist density was $9000 \text{ turns m}^{-1}$.

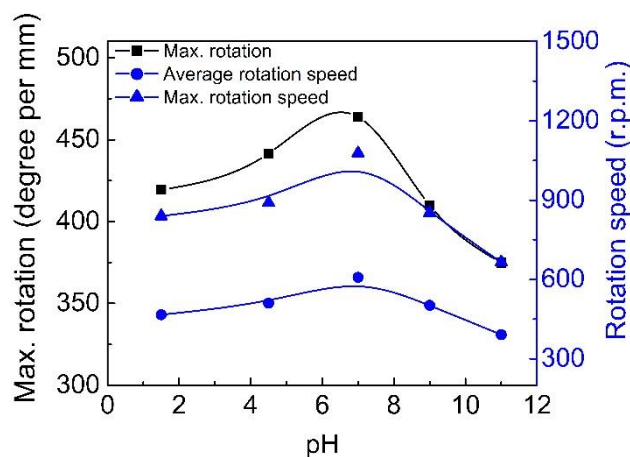


Figure S19. Torsional stroke, maximum rotation speed, and average rotation speed for silk muscles driven by different pH water fog of $0.22 \text{ g s}^{-1} \text{ m}^{-2}$. The muscle investigated is the same type as for Figure S16.

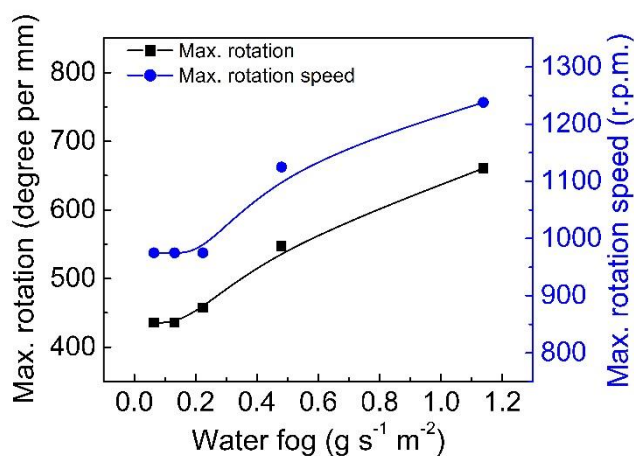


Figure S20. Dependence of torsional stroke and maximum rotation speed on concentration of water fog for a torsional silk muscle at room temperature. The muscle investigated is the same type as for Figure S16.

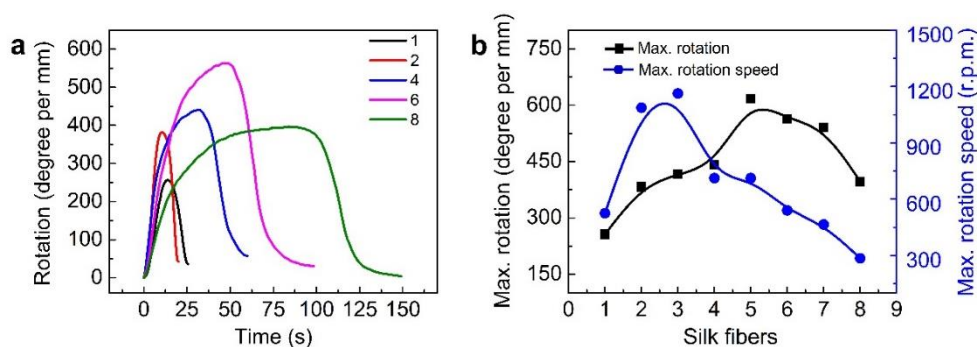


Figure S21. a) Time dependence of torsional actuation for torsional silk muscles made from plying different numbers of dual-filament silk fibers, when actuated by water fog of $0.22 \text{ g s}^{-1} \text{m}^{-2}$. b) Maximum rotation speed and torsional stroke of the silk muscles as a function of the number of plied dual-filament silk fibers.

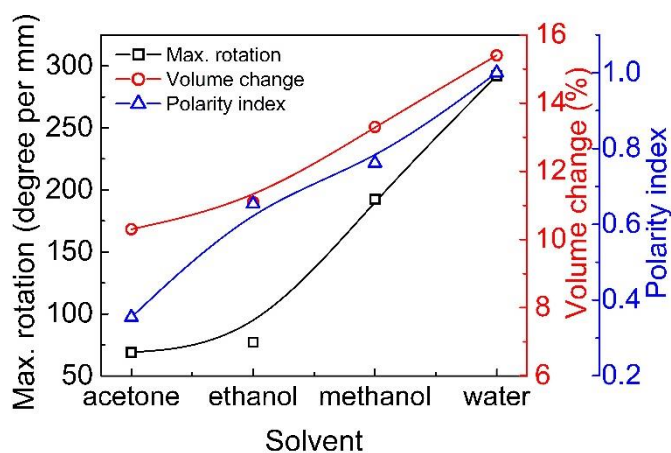


Figure S22. Comparison of torsional stroke and volume changes driven by different solvent vapors of $73.4 \text{ mL s}^{-1} \text{ m}^{-2}$ for 0.3 s for a silk muscle under isobaric stress of 1.1 MPa. The muscle investigated is the same type as for Figure S16.

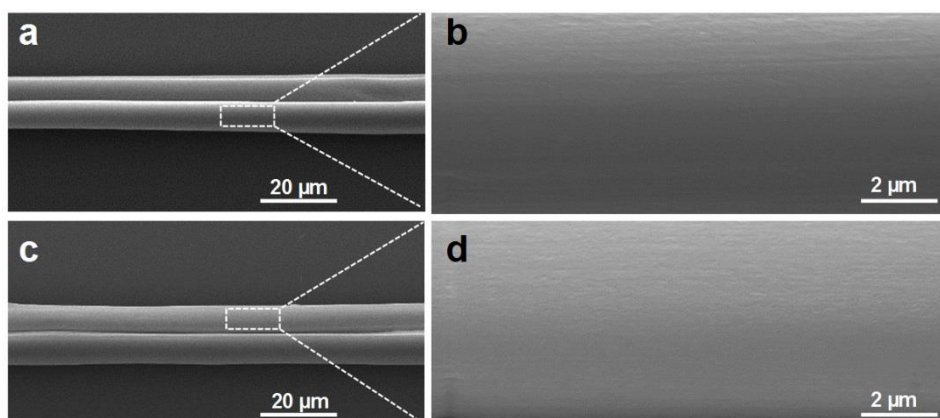


Figure S23. SEM images of a dual-filament, NaOH-degummed silk fiber before (a, b) and after (c, d) thermal annealing ($120 \text{ }^{\circ}\text{C}$ in air for 10 minutes), at low and high magnifications. There was no obvious change in the surface topography of the silk fiber as a result of thermal annealing.

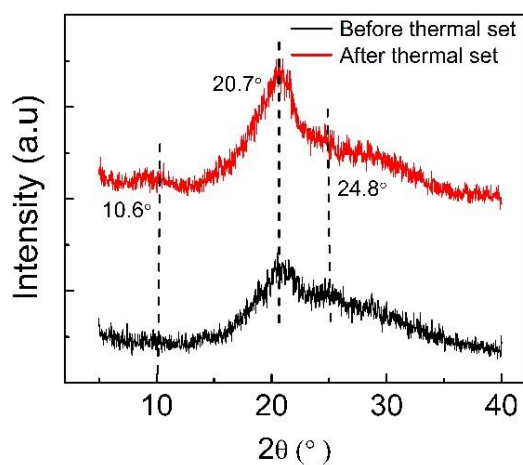


Figure S24. X-ray diffraction (CuK α radiation) of NaOH-degummed silkworm silk before and after thermal annealing (120 °C in air for 10 minutes). These results show that thermal annealing increases the crystallinity of the silk fiber.

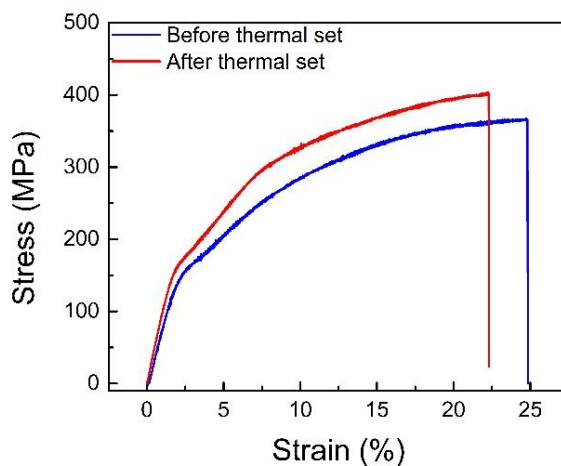


Figure S25. Typical stress-strain curves of the silk fibers before (blue) and after (red) thermal treatment at 120 °C in air for 10 minutes. The tests were conducted under ambient conditions of ~20% humidity at 25 °C. The twist density of the silk fiber was 6000 turns m^{-1} .

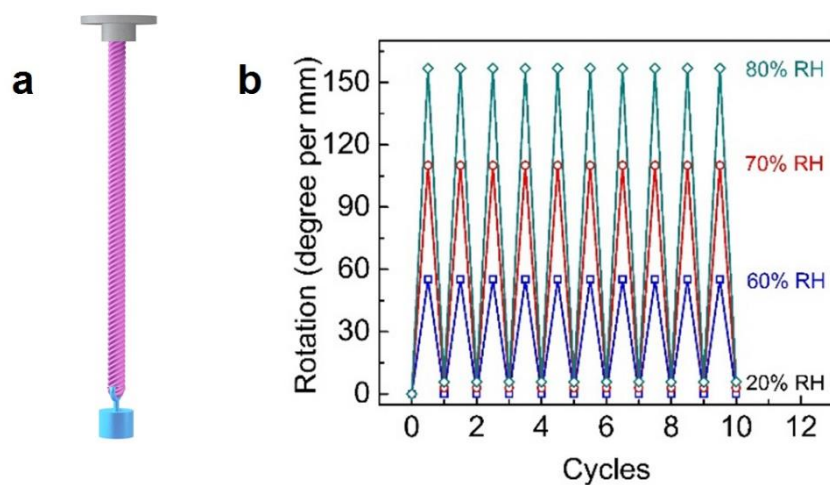


Figure S26. a) Schematic illustration of a thermally-set torsional silk muscle. b) Torsional stroke change during selected humidity-change cycles from 20% RH to different humidities for a one-end-tethered silk muscle that had been thermally-set at 120 °C in air for 10 minutes. The twist density of the silk fiber was 6000 turns m^{-1} , the muscle diameter was 14 μm , and the weight of the paddle was 50.0 mg.

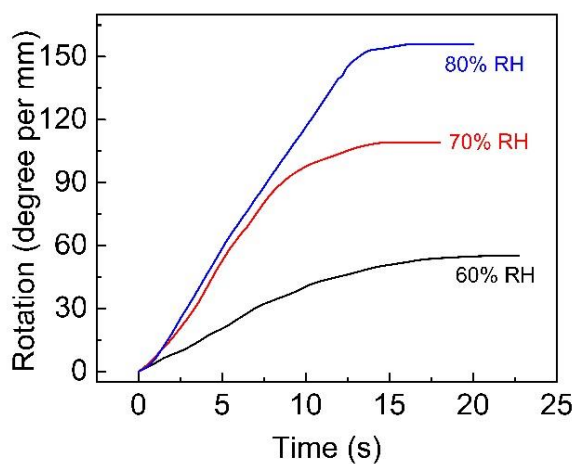


Figure S27. Time dependence of torsional actuation for the thermally-set torsional muscle described in Figure S24.

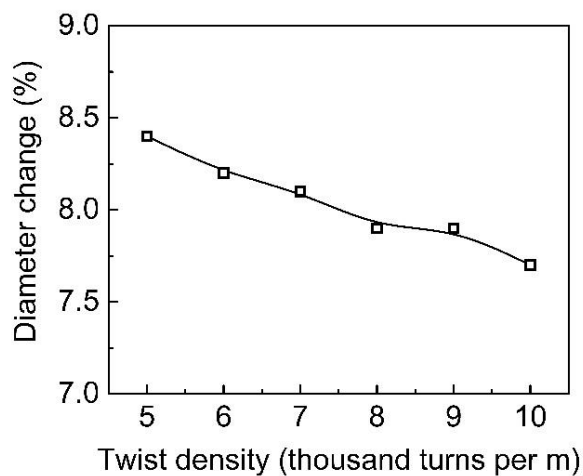


Figure S28. Diameter change of a silk fiber as a function of the amount of inserted twist when RH was changed from 20% to 80% at room temperature. The investigated $\sim 14\text{-}\mu\text{m}$ -diameter silk fiber muscle was single-ply and torque balanced (because of heat setting), and then heat-set at $120\text{ }^{\circ}\text{C}$ in air for 10 minutes.

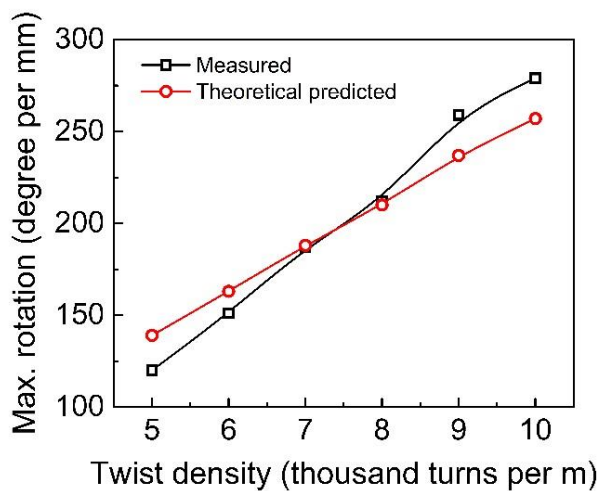


Figure S29. Comparison of measured (black squares) and theoretically-predicted (red circles, obtained using Equation 3) torsional stroke as a function of applied twist density for a thermally-set silk muscle ($120\text{ }^{\circ}\text{C}$ in air for 10 minutes). The torsional actuation was driven by a RH change from 20% to 80%.

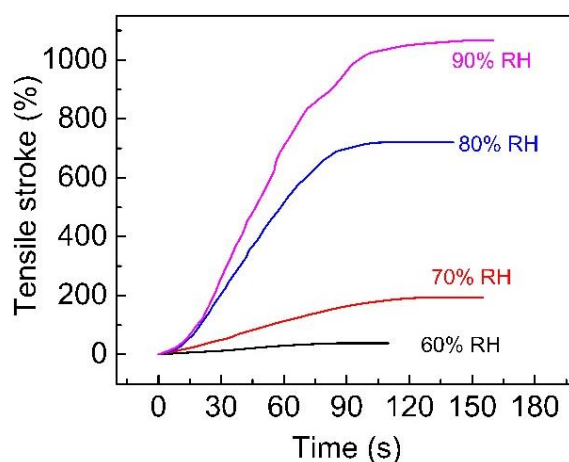


Figure S30. Time dependence of tensile stroke at room temperature for a ZS silk muscle without load when relative humidity was changed from 20% to different other humidity values. The silk muscle was fabricated by twisting five dual-filament silk fibers to a twist density of $6000 \text{ turns m}^{-1}$. The spring index was 7.5.

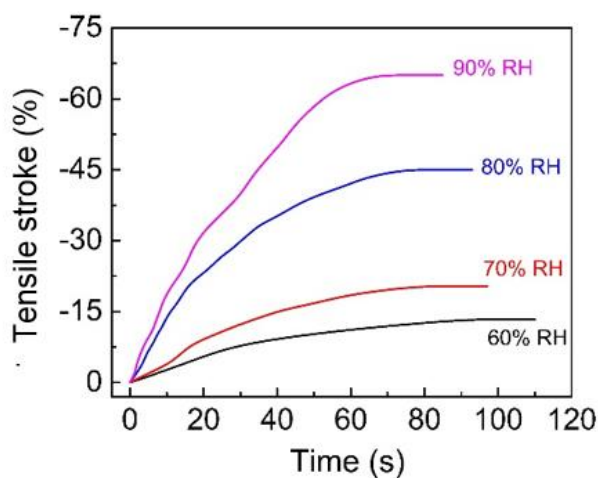


Figure S31. The time dependence of tensile stroke at room temperature for a ZZ silk muscle without load when relative humidity was changed from 20% to different other humidity values. The silk muscle was fabricated by twisting five dual-filament silk fibers to a twist density of $6000 \text{ turns m}^{-1}$. The spring index was 7.5.

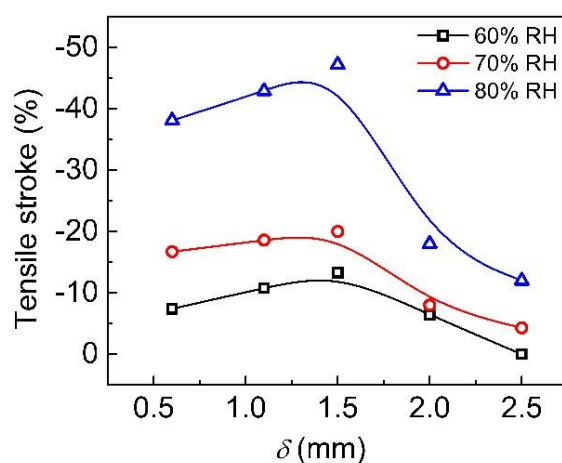


Figure S32. The dependence of tensile stroke at room temperature on coil pitch (δ) for homochiral silk muscles without load when the relative humidity was changed from 20% to various other relative humidities. The silk muscles were made by twisting five dual-filament silk fibers to a twist density of $6000 \text{ turns m}^{-1}$. All muscles had spring index of 7.5.

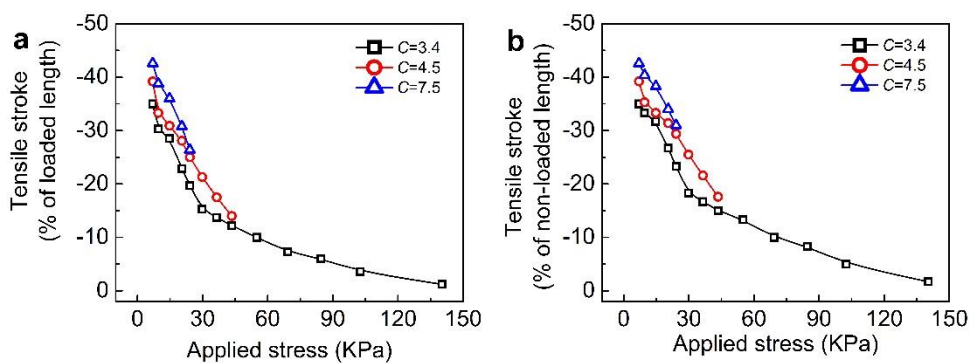


Figure S33. a) Stress dependence of tensile stroke as percent of the loaded muscle length for SS silk muscles with different spring indexes when the room temperature relative humidity was changed from 20% to 80%. b) The results of A when normalized to the initial non-loaded muscle length.

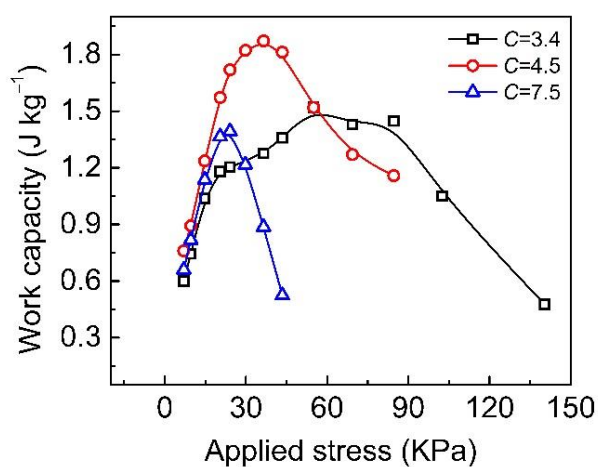


Figure S34. Stress dependence of work capacity for SS silk muscles with different spring indexes when room temperature relative humidity was changed from 20% to 80%.

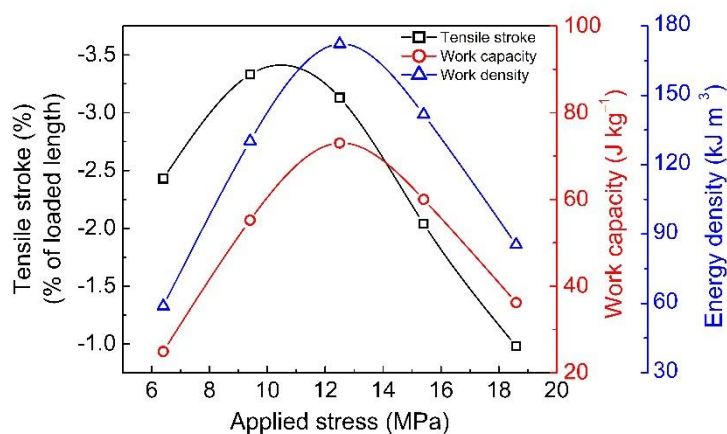


Figure S35. Tensile stroke, work capacity and energy density for a two-end-tethered self-assembly coiled silk yarn with an applied isobaric load driven by water droplets. The silk yarn had a diameter of 262 μm and a spring index of 1.8.

Table S1. Effects of water on three models.

Model	Quantification parameter	Fully dehydrated	Fully hydrated
3PUB	Hydrogen bond	548.56 ± 0.0731	381.72 ± 0.1865
	Interaction energy (kJ mol ⁻¹)	-75103.32 ± 1.9333	-63640.04 ± 7.7214
	Gyration radius (nm)	1.7879 ± 0.00003	1.8645 ± 0.0001
	Volume (nm ³)	161.5802	213.1250
	Chain COM distance (nm)	4.4085	4.9671
	Amino acids residues of secondary structure	220	260
2FJY	Hydrogen bond	296.92 ± 0.0551	296.92 ± 0.0551
	Interaction energy (kJ mol ⁻¹)	200.16 ± 0.1650	200.16 ± 0.1650
	Gyration radius (nm)	-41897.36 ± 0.9981	-41897.36 ± 0.9981
	Volume (nm ³)	115.8354	160.4585
	Chain COM distance (nm)	3.2	3.5
	Amino acids residues of secondary structure	130	160
3UA0	Hydrogen bond	190.01 ± 0.0411	190.01 ± 0.0411
	Interaction energy (kJ mol ⁻¹)	112.01 ± 0.1202	112.01 ± 0.1202
	Gyration radius (nm)	-60274.35 ± 1.007	-60274.35 ± 1.007
	Volume (nm ³)	79.04925	120.8959
	Amino acids residues of secondary structure	46	85

* The chain COM distance stands for the distance between the center of mass of two chains in the system. This parameter is for 3PUB and 2FJY model since 3UA0 only contains one chain.

Table S2. Evolution of the secondary structure in each model.

Model	Secondary structure	Fully dehydrated	Fully hydrated
3PUB	α-helix	22%	31%
	β-sheet	28%	35%
2FJY	α-helix	45%	63%
	β-sheet	1%	1%
3UA0	α-helix	0%	0%
	β-sheet	40%	67%

*The percentage of each component is the ratio between atom number of secondary structure and whole system.

Table S3. Comparison of torsional rotation between silk muscle and previously reported hygromorph muscles.

Materials	Silkworm muscle (This work)	silk	PEDOT:PS S/ CNT hybrid yarn ^[6]	Graphene hydrogel fiber ^[7]	Multi-ply plasma-treated MWCNT yarn muscle ^[8]
Stimulus	Water fog		Water	Humidity	Water
Diameter (μm)	19		30	62	40
Torsional rotation ($^\circ \text{mm}^{-1}$)	547		1399	588	61.3
Peak velocity (r.p.m.)	1125		1395	5190	–
Normalized peak velocity (r.p.m. per meter)	11250		31000	25950	–
Initial specific torque (N m kg^{-1})	0.063		0.52	0.082	0.4
Two-end-tethered	no		no	no	yes

Table S4. Comparison of torsional actuation performance for fiber muscles made from different commercial fiber materials driven by water fog of $0.22 \text{ g s}^{-1} \text{ m}^{-2}$.

Material	Silkworm silk ^[9]	Cotton	Flax	Wool	Tencel	Bamboo fiber	Polyester	Nylon 6,6	Spandex
Twist density (turns m^{-1})	6000	4771	5176	4771	6828	7071	1267	4213	4526
Diameter (μm)	13.2	16.6	15.3	16.6	11.6	11.2	62.5	18.8	17.5
Twist density \times Diameter (100 turns $\text{m}^{-1} \times \mu\text{m}$)	792	792	792	792	792	792	792	792	792
Applied stress (MPa)	1.7	1.7	1.7	1.7	1.7	1.7	1.7	1.7	1.7
Rotation ($^\circ \text{mm}^{-1}$)	216	153	126	36	225	234	0	0	0
Average rotation speed (r.p.m)	133	36	33	3.6	16	56	–	–	–
Reversible	yes	yes	yes	yes	yes	yes	–	–	–

*All the torsional muscles were made using the same process as the silk muscle.

Table S5. Comparison of tensile performance for fiber muscles made from different commercial fiber materials.

Materials	Thermal setting	Humidity-driven	Reversible	Contraction (20%–80% RH)	Response time (s)	Response rate (% s ⁻¹)
Silk	yes	yes	yes	47	160	0.29
Cotton	yes	yes	yes	13	90	0.14
Wool	yes	yes	yes	23	100	0.23
Tencel	yes	yes	yes	32	100	0.32
Modal/cotton	yes	yes	yes	20	110	0.18
Spandex	yes	no	–	–	–	–
Nylon 6,6	yes	no	–	–	–	–
Polyester	yes	no	–	–	–	–
polypropylene fiber	yes	no	–	–	–	–
polyacrylonitrile fiber	yes	no	–	–	–	–

*All the tensile muscles were made using the same process as the silk muscle with a same spring index of 4.3 and an intercoil spacing of 1.3mm.

Table S6. Comparison of tensile stroke between silk yarn muscle and previously reported water or hygromorph muscles.

Materials	Silk muscle (This work)	PDDA/CNT hybrid yarn ^[10]	Graphene oxide fiber ^[11]	PEDOT:PSS /CNT hybrid yarn ^[6]	CNT/silk fiber ^[12]	Spider silk ^[13]
Stimulus	Humidity	Water or humidity	Humidity	Water	Humidity	Humidity
Diameter (μm)	82	67	34	30	6.5	5
Maximum contraction (%)	70	78	5	68	0.4	0.5
Response time (s)	67	720	10	–	240	2
Response rate (% s ⁻¹)	1.04	0.72	0.5	–	0.0017	0.025
Two-end-tethered	no	yes	no	yes	no	no
Maximum work capacity (J kg ⁻¹)	73*▲	2170*	–	96.9	–	–

▲ The two ends of the muscle were tethered in the measurement.

* The value and other results came from different samples for a kind of muscle.

Movie S1. A crawling artificial “caterpillar” made of a coiled silk muscle on a barbed wire, which was driven by moisture of a finger. The tensile silk muscle was made from five twisted dual-filament silk fibers with a spring index of 7.5.

Movie S2. A smart textile woven from silk fiber muscles, which responds to humidity change in the environment by contracting during water absorption and then expanding upon water desorption.

Movie S3. Animated display of smart clothes which change macroshape or microstructure to achieve moisture and thermal management for increased comfort between skin and fabric.

Supporting References

- [1] P. Jiang, H. Liu, C. Wang, L. Wu, J. Huang, C. Guo, *Mater. Lett.* **2006**, *60*, 919.
- [2] a) S. Ling, Z. Qi, D. P. Knight, Z. Shao, X. Chen, *Biomacromolecules* **2011**, *12*, 3344; b) H. H. Kim, M. K. Kim, K. H. Lee, Y. H. Park, I. C. Um, *Int. J. Biol. Macromol.* **2015**, *79*, 943.
- [3] M. Li, S. Lu, Z. Wu, H. Yan, J. Mo, L. Wang, *J. Appl. Polym. Sci.* **2001**, *79*, 2185.
- [4] M. D. Lima, N. Li, M. Jung de Andrade, S. Fang, J. Oh, G. M. Spinks, M. E. Kozlov, C. S. Haines, D. Suh, J. Foroughi, S. J. Kim, Y. Chen, T. Ware, M. K. Shin, L. D. Machado, A. F. Fonseca, J. D. W. Madden, W. E. Voit, D. S. Galvão, R. H. Baughman, *Science* **2012**, *338*, 928.
- [5] J. Pérez-Rigueiro, C. Viney, J. Llorca, M. Elices, *J. Appl. Polym. Sci.* **2000**, *75*, 1270.
- [6] X. Gu, Q. Fan, F. Yang, L. Cai, N. Zhang, W. Zhou, W. Zhou, S. Xie, *Nanoscale* **2016**, *8*, 17881.
- [7] H. Cheng, Y. Hu, F. Zhao, Z. Dong, Y. Wang, N. Chen, Z. Zhang, L. Qu, *Adv. Mater.* **2014**, *26*, 2909.
- [8] S. He, P. Chen, L. Qiu, B. Wang, X. Sun, Y. Xu, H. Peng, *Angew. Chem.* **2015**, *127*, 15093.
- [9] H. J. Jin, D. L. Kaplan, *Nature* **2003**, *424*, 1057.
- [10] S. H. Kim, C. H. Kwon, K. Park, T. J. Mun, X. Lepró, R. H. Baughman, G. M. Spinks, S. J. Kim, *Sci. Rep.* **2016**, *6*, 23016.
- [11] H. Cheng, J. Liu, Y. Zhao, C. Hu, Z. Zhang, N. Chen, L. Jiang, L. Qu, *Angew. Chem.* **2013**, *52*, 10482.
- [12] E. Steven, W. R. Saleh, V. Lebedev, S. F. Acquah, V. Laukhin, R. G. Alamo, J. S. Brooks, *Nat. Commun.* **2013**, *4*, 2435.
- [13] I. Agnarsson, A. Dhinojwala, V. Sahni, T. Blackledge, *J. Exp. Biol.* **2009**, *212*, 1990.